EXPERIMENTAL AND NUMERICAL INVESTIGATION OF BALLISTIC IMPACT BEHAVIOUR OF HIGH STRENGTH ALUMINIUM PLATES

A THESIS SUBMITTED TO
THE GRADUATE SCHOOL OF NATURAL AND APPLIED SCIENCES
OF
MIDDLE EAST TECHNICAL UNIVERSITY

BY

GÜRALP BAŞARAN

IN PARTIAL FULFILLMENT OF THE REQUIREMENTS
FOR
THE DEGREE OF MASTER OF SCIENCE
IN
AEROSPACE ENGINEERING

DECEMBER 2019

Approval of the thesis:

EXPERIMENTAL AND NUMERICAL INVESTIGATION OF BALLISTIC IMPACT BEHAVIOUR OF HIGH STRENGTH ALUMINIUM PLATES

submitted by **GÜRALP BAŞARAN** in partial fulfillment of the requirements for the degree of **Master of Science in Aerospace Engineering Department, Middle East Technical University** by,

Prof. Dr. Halil Kalıpçılar
Dean, Graduate School of **Natural and Applied Sciences** _____

Prof. Dr. İsmail Hakkı Tuncer
Head of Department, **Aerospace Engineering** _____

Assoc. Prof. Dr. Ercan Gürses
Supervisor, **Aerospace Engineering, METU** _____

Examining Committee Members:

Prof. Dr. Altan Kayran
Aerospace Engineering, METU _____

Assoc. Prof. Dr. Ercan Gürses
Aerospace Engineering, METU _____

Assoc. Prof. Dr. Demirkan Çöker
Aerospace Engineering, METU _____

Assoc. Prof. Dr. Melin Şahin
Aerospace Engineering, METU _____

Assist. Prof. Dr. Recep M. Görgülüarslan
Mechanical Engineering, TOBB _____

Date:

I hereby declare that all information in this document has been obtained and presented in accordance with academic rules and ethical conduct. I also declare that, as required by these rules and conduct, I have fully cited and referenced all material and results that are not original to this work.

Name, Surname: GÜRALP BAŞARAN

Signature :

ABSTRACT

EXPERIMENTAL AND NUMERICAL INVESTIGATION OF BALLISTIC IMPACT BEHAVIOUR OF HIGH STRENGTH ALUMINIUM PLATES

BAŞARAN, GÜRALP
M.S., Department of Aerospace Engineering
Supervisor: Assoc. Prof. Dr. Ercan Gürses

December 2019, 90 pages

A hybrid solution method was used to examine the ballistic collision situation to be used in armored vehicle design. This hybrid solution method includes an Artificial Neural Network (ANN) and a Finite Element (FE) solver. MATLAB was used for ANN model, and LSDYNA® was used as FE solver. For this purpose, first ballistic tests were performed, and projectile residual velocities and depth of penetrations were measured. The FE model was confirmed by ballistic tests. After the FE model validation, FE analyses were performed for different armor thicknesses, and the results were transferred in the ANN model. The ANN model and FE method results were compared for different armor thicknesses, and the ANN model was validated. The validated ANN model was transferred to MATLAB® SIMULINK® and a tool that is capable of predicting the results of ballistic collision in a short time.

Keywords: ballistics, armor, bullet, Finite Element Analysis, neural network

ÖZ

YÜKSEK MUKAVEMETLİ ALÜMİNYUM LEVHALARIN BALİSTİK ÇARPMA DAVRANIŞLARININ DENEYSEL VE SAYISAL OLARAK İNCELENMESİ

BAŞARAN, GÜRALP
Yüksek Lisans, Havacılık ve Uzay Mühendisliği Bölümü
Tez Yöneticisi: Doç. Dr. Ercan Gürses

Aralık 2019 , 90 sayfa

Zırhlı araç tasarımında kullanılmak üzere, balistik çarpışma durumunu incelemek için hibrit bir çözüm metodu kullanılmıştır. Bu hibrit çözüm yöntemi, Yapısal Sinir Ağı (YSA) ve Sonlu Elemanlar (SE) çözücüsünü içermektedir. YSA modeli için MATLAB, SE çözücüsü olarak da LSDYNA® kullanılmıştır. Bu amaçla, ilk olarak balistik testler gerçekleştirilmiş, mermi çıkış hızları ve giriş derinlikleri ölçülmüştür. Gerçekleştirilen balistik testler ile SE modeli doğrulanmıştır. SE modeli doğrulamasından sonra, farklı zırh kalınlıkları için SE analizleri yapılmış ve sonuçlar YSA modelinde kullanılmak üzere kaydedilmiştir. Farklı zırh kalınlıkları için YSA modeli ve SE yöntemi sonuçları karşılaştırılmış ve YSA modelinin doğrulaması yapılmıştır. Doğrulanan YSA modeli MATLAB® SIMULINK®'e aktarılmış ve balistik çarpışma sonuçlarını kısa sürede tahmin edebilen bir gereç yapılmıştır.

Anahtar Kelimeler: balistik, zırh, mermi, Sonlu Eleman Analizleri, Yapısal Sinir Ağ

Dedicated to my family

ACKNOWLEDGMENTS

First and foremost, I would like to express my gratitude to my supervisor Assoc. Prof. Dr. Ercan Gürses for his constant support, guidance and patience throughout the preparation of this study.

Besides my supervisor, I would like to thank the rest of my thesis committee: Prof. Dr. Altan Kayran, Assoc. Prof. Dr. Demirkan Çöker, Assoc. Prof. Dr. Melin Şahin and Dr. Recep Görgülüaslan, for their insightful comments and contributions during thesis defense.

I would like to give my special thanks to Erkal Özbayramoğlu, Onur Bütün, Eren Öney and İlker Kurtoğlu for their support. They have always been there for me whenever I needed help.

Lastly, I also would like to thank my wife Esra Başaran and my parents Perihan Başaran and Gazi Başaran for their caring and love throughout all the time. Their encouragement and support brought me to these days.

TABLE OF CONTENTS

LIST OF TABLES

TABLES

LIST OF FIGURES

FIGURES

CHAPTER 1

INTRODUCTION

1.1 Ballistic Impact

Ballistics is a branch of science that examines the situation of ammunition from the moment of the exit from the barrel until the collision with the target. Much effort has been spent in recent years to understand and mathematically express the physics at the moment of collision. The examination of ballistic impact with a computer-aided approach has been developed over the years. New demands of ground forces are faster and more agile transportation from one point to another with safe occupants. Impact studies are mainly focusing on two main subjects, which are vulnerability and survivability requirements. Vulnerability and survivability criteria also contain equipment protection, which can be a risk for the personal and critical for the vehicle. Plastic deformation, fracture mechanics, wave propagation, contact mechanics, and thermodynamics are all involved with the highly non-linear and complex ballistic impact phenomena. During a ballistic collision, large strain and strain rate hardening mechanisms work together with thermal softening mechanisms. Temperature levels can go beyond the melting point, and strain rate levels are above 1000 s^{-1}. Generally, processes end in 30μs and projectile initial velocities are above 600 m/s. The first chapter is mainly about the classification of ballistic collisions, projectile and target types, and reaction characteristics of a target under high-velocity impact at changing strain rates. In the second section, the technical terms used in ballistic impact studies will be explained. Definitions of the ballistic limit, the fragment simulating projectile, the aerial density are given, and the physics of impact is shortly explained.

1.2 Types of Ballistic Collision and Projectiles and Target

Mainly, the ballistic collision is classified using parameters such as the angle of incidence of impact, material properties, impact velocities, etc. The main characteristics of penetration and perforation mechanisms are defined with the speed of a bullet. Therefore, most commonly, the initial velocity of a projectile is used for the classification.

1.2.1 Categorization of Ballistic Collision Types

There are two main groups concerning projectile impact velocity for the categorization of ballistic impact, which is used in military applications and engineering. In Table 1.1 the classification of ballistic impact is given [1].

Table 1.1: Classification of ballistic impact [1]

Ballistic impact	Classification	Velocity Range V_s(m/s)	Example
Military application	Sub ordnance	25-500	Drop tests
	Nominal ordnance or ordnance	500-1300	Propellant fired conventional gun
	Ultra-ordnance	1300-3000	Warhead Fragments
	Hypervelocity	>3000	Shaped Charge
General Application	Low/moderate velocity impact	<50	Automobile Crashes
	High-velocity impact	50-1500	Projectile impacts, bird strike in aircraft engines, etc.
	Hypervelocity impact	>1500	Debris impact on satellites

Subgroups of ballistic collision categorization are mainly based on the strike velocity of the projectile. In military applications, there are four main strike velocity ranges, so-called sub-ordnance, nominal ordnance, ultra-ordnance, and hypervelocity. Their corresponding velocity ranges are given in Table 1.1. In order to perform sub-ordnance ballistic tests, pneumatic guns can be used. For a nominal ordnance test, commonly conventional guns are used. Finally, for ultra-ordnance and hypervelocity strike velocity ranges, special purpose guns and light-gas guns can be employed, respectively.

In general applications, crashworthiness studies of vehicles are performed in veloc-

ity ranges less than 50 m/s, which refers to the low/moderate velocity impact range. The high-velocity impact is encountered, for example, in projectile impacts and bird strikes. Finally, space shuttles and satellites have requirements against meteor impacts, which are examples of a hypervelocity impact.

1.2.2 Projectile Types

Projectiles may have different forms, depending on their main body structure and tip shapes. Table 1.2 summarizes the common projectile types.

Table 1.2: Classification of projectile shape [1]

Projectile	Shape
Main Body	Sphere
	Solid rod or bar
	Hollow Shell
	Irregular Solid
	Solid rod with two or three different core materials
Nose or frontal portion	Conical
	Ogival
	Hemi-spherical
	Flat

1.2.3 Target Types

In 1978, Backman and Goldsmith divided target types into four groups, which are given in Table 1.3. Their classification of target types is based on the ratio of the thickness (h_t) to the diameter (D) of the projectile.

Table 1.3: Classification of target [1]

Target Classification	Ratio of h_t/D
Thin	< 1
Intermediate	1-8
Thick	8-12
Semi-infinite	> 12

1.3 The ballistic response of materials

When the impact velocity of a projectile is between 500m/s and 2000m/s global deformation characteristics of target material becomes less important. Relatively large and localized deformations are observed in the neighborhood of impact area (about 3-4 times of bullet diameter) while the rest of the target remains almost undeformed. The deformed shape of a target after impact is shown in Figure 1.1 for a better understanding.

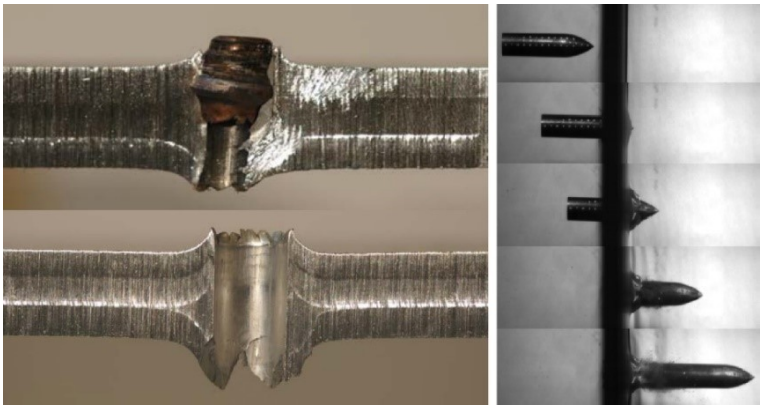

Figure 1.1: Deformed shape of target after strike and perforation process [4].

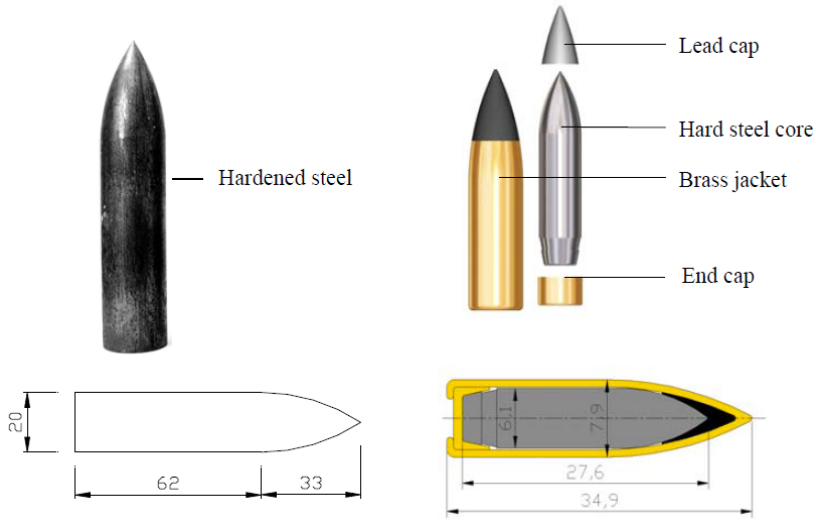

Figure 1.2: Geometry and dimensions (in mm) of 20mm ogive-nose hardened steel projectile(left) and 7.62mm APM2 bullet (right) [4].

Børvik et al. [4] studied the perforation process of aluminum 5083-H116 armor plate. Figure 1.2 shows the geometry and dimensions (in mm) of 20mm ogive-nose hardened steel projectile (left), and 7.62mm APM2 bullet (right) [4]. Plates of various thicknesses were used in this study for a range of 480-950m/s striking velocities. A comparison was made among ogival, nose-shaped, and 7.62mm APM2 projectiles in terms of perforation processes. It was shown that the effect of lead brass and jacket are negligible for residual velocity values compared to other nose-shaped bullets. Residual velocity is velocity value after the finishing of perforation.

Table 1.4 shows the upper and lower boundaries of strike velocity values concerning their strain rate levels. These velocity values can be taken as reference points for the classification.

The impact response of a bullet is directly related to stress waves which are generated during the impact. These stress waves are functions of parameters such as velocity, geometry, strain rate, material, localized plastic flow, etc. The response time of collided parts is in the range of microseconds for all ballistic impacts.

Table 1.4: Response of materials under the ballistic impact [2]

Strain rate s^{-1}	Impact velocity(m/s)	Effect or material response
0 - 10^0	< 50	Primarily elastic and some local plasticity
10^0 - 10^2	50-500	Primarily plastic
10^2 - 10^4	500-1000	Viscous – material strength still significant
10^4 - 10^5	1000-3000	Fluid like behavior in materials; pressures approach or exceed material strength; density a dominant parameter
10^5 - 10^7	3000-12000	Hydrodynamic behavior - material compressibility not ignorable
10^7 - above	>12000	Explosive impact-colliding solids get vaporized

1.4 Penetration Mechanics

The definition of penetration is the entrance of the missile or penetrator into a target after the collision, without exiting the target body. Bouncing back of a bullet or burying into a target case is also included in the ballistic impact. During a collision, the energy of the projectile is transferred to strain energy, energy loss due to friction (i.e., heat, sound, light) of collided parts. The determination of the kinetic energy of a projectile is essential for penetration analysis. There is not an easy way to measure the amounts of these energies. To simplify the analyses, some assumptions/approximations about the energies of collided parts must be made.

Penetration process can be grouped into four stages [1]:

1. Transient
2. Primary penetration
3. Secondary Penetration
4. Recovery

The first stage is the initial contact of the impactor with the target interface. The maximum value of pressure is attained in the transient stage of impact. In the primary

penetration stage, the impactor starts to use its driving force into a target, and material starts to behave fluid-like material locally at the interface. The secondary penetration phase starts with the end of the deformation of the bullet.The deformation of the target by the projectile's kinetic energy is not considered in this phase. Instead, a shockwave which is distributed by the impactor deforms the target. The last stage of penetration is the recovery phase in which the shrinkage of the crater takes place.

The conservation of energy law holds during a collision. The impact energy of the bullet transforms into the internal energy and the kinetic energy of the target together with some forms of energy losses.

$$\mathrm{E_{trans}} = \mathrm{E_{plate}} + \mathrm{KE_{plate}} + \mathrm{IE^{eroded}} + \mathrm{KE^{eroded}} \tag{1.1}$$

In the above equation where $\mathrm{E_{trans}}$ denotes the total energy transmitted, subscript 'plate' refers to the energy of the plate; and the superscript 'eroded' denotes the energy in the eroded mass [1]. $\mathrm{E_{plate}}$ represents the strain energy of the plate, $\mathrm{IE^{eroded}}$ is the internal energy of the eroded parts and $\mathrm{KE_{plate}}$ is the kinetic energy of the plate.

1.5 Limit Velocities

The impact velocity and the thickness of the target determine the failure mode of collided parts. Limit velocities are grouped into three, which are the elastic limit velocity, the plastic limit velocity, and the hydrodynamic limit velocity.

1.5.1 Elastic Limit Velocity

The elastic limit velocity, $\mathrm{V_{EL}}$, is the maximum velocity, which creates only elastic deformation both in the projectile and the target. This situation can only happen at very low impact speeds. In case of a flat nose-shaped bullet, or a planar contact surface at the interface of impact, compressive stress equal to the yield stress σ_{yc} is

generated, and the elastic limit velocity is computed as given in Eq. (1.2)

$$\mathrm{V_{EL}} = \frac{\sigma_{\mathrm{yc}}\left[\rho_{\mathrm{t}}\mathrm{c_{1t}} + \rho_{\mathrm{p}}\mathrm{c_{0p}}\right]}{\left(\rho_{\mathrm{t}}\mathrm{c_{1t}}\rho_{\mathrm{p}}\mathrm{c_{0p}}\right)} = \frac{\sigma_{\mathrm{yc}}[\mathrm{Z_{1t}} + \mathrm{Z_{0p}}]}{\mathrm{Z_{1t}Z_{0p}}} \tag{1.2}$$

where,

$$\mathrm{c_1} = \sqrt{\frac{\lambda + 2\mathrm{G}}{\rho}}, \mathrm{G} = \frac{0.5\mathrm{E}}{1+\nu}, \mathrm{c_0} = \sqrt{\frac{\mathrm{E}}{\rho}} \tag{1.3}$$

In Eqs. (1.2) and (1.3), $\mathrm{c_1}$ and $\mathrm{c_0}$ represent the wave velocities $\mathrm{Z_1}$ and $\mathrm{Z_0}$ are impedances of in longitudinal and transverse directions and λ is the Lame's constant. E is Young's modulus, G is the shear modulus, ν is the Poisson's ratio, ρ is the mass density, and subscripts p and t denote the projectile and the target, respectively [11].

1.5.2 Plastic Limit Velocity

Plastic limit velocity, $\mathrm{V_{PL}}$ (see Eq. (1.4)), is the maximum velocity, which leads to a perdurable deformation on both target and impactor. For a steel with a compressive strength of 152MPa and and tensile strength of 250MPa, the $\mathrm{V_{EL}}$ is 3.75m/s and the $\mathrm{V_{PL}}$ is 90m/s [1]. At the plastic limit velocity, plastic stresses are less than hydrodynamic stresses.

$$V_{PL} = \sqrt{\frac{\sigma_y}{\rho}} \tag{1.4}$$

Figure 1.3 shows an impact case without projectile drilling into a target. In this case, two types of failure modes are activated because of plastic deformations. The first mode occurs at the contact interface between the bullet and the target, which is called bulging. In this mode, the contact surface of the target takes the form of a projectile nose shape. The second mode is activated by bending, referred to as dishing, which might widen far from the impact interface [5].

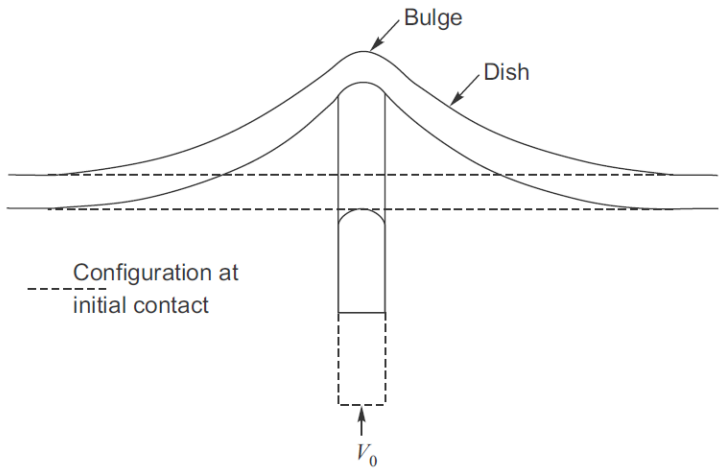

Figure 1.3: Permanent deformations of thin target element showing bulging and dishing [1].

1.5.3 Hydrodynamic Limit Velocity

The hydrodynamic limit velocity, V_{HL} defines this maximum strike velocity just before shock waves occur both in the projectile and the target. The whole deformation process starts with plastic limit velocity and ends with hydrodynamic limit velocity. This limit velocity can be related to the bulk modulus, K, of the material as given in Eq. (1.5)

$$V_{HL} = \sqrt{\frac{K}{\rho}} \tag{1.5}$$

It is considered that, above the hydrodynamic speed limit, the compressibility of the solid decreases, and therefore, shock waves occur. Also, at sufficiently high, impact velocities (e.g.,> $3V_{HL}$) [11], phase changes, vaporization, or even impact explosions may be expected [12], [13].

1.6 Ballistic Limit and Aerial Density

Ballistic limit evaluation is a fundamental concept in order to determine the performance of an armor. A good quality armor design has a high ballistic limit. The ballistic limit is defined as an average of the fully perforating velocity and the partial penetrating velocity.

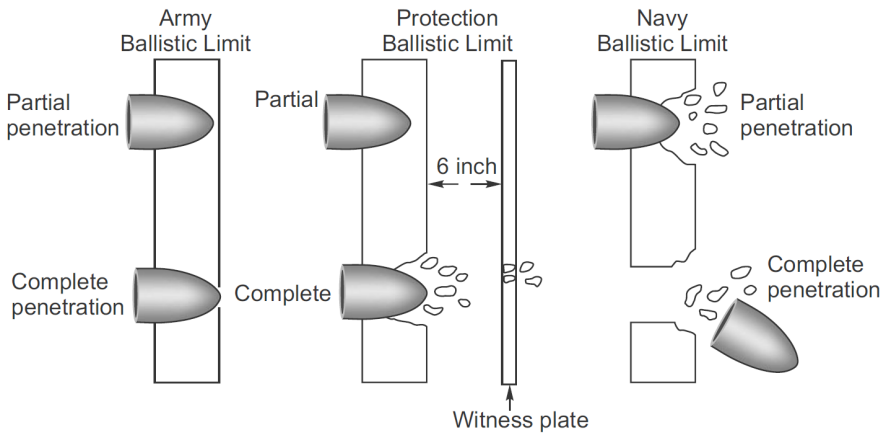

Figure 1.4: Definitions of perforation and partial penetration for defining the ballistic limit [5].

There are several measurement criteria for ballistic limit determination. Most commonly used criteria are:

1. Army ballistic limit
2. Protection ballistic limit
3. Navy ballistic limit

Above listed criteria are illustrated in Figure 1.4 [5]. The main objective of the ballistic limit tests is to determine the velocity of the projectile, which fails to perforate in the target. This velocity can be obtained either using physical principles (i.e., conservation law and material relations) or probabilistic methods which are based on an immense database of striking velocities. Details on deterministic and probabilistic methods for ballistic determination limit can be found in [5].

1.7 Literature Survey on ballistic FEA combined ANN studies

One of the most critical subjects in the defense industry is the ballistic protection. Numerical methods have been widely used for the determination of the ballistic limit. Furthermore, analytical and empirical solutions are widely used for ballistic problems. Analytical models and empirical equations are generated from numerous experiments and are employed as a solution method for ballistic collision problems [14]. Since empirical formulations are case-specific, they are generally not valid for different cases. They must be derived for each problem, and this derivation is complicated and costs too much time.

Analytical models can be used on various problems directly. They are convenient for ballistic problems. However, their derivations involve simplifications, which then leads to differences in outcomes [2].

In a conclusion, one can see that determination of the impact characteristics is a very complicated task, and generally, it cannot be determined using the analytical and empirical. At this point, FEA is an alternative tool to model the ballistic impact. With the help of the developments in FEA and computational resources, these complex impact phenomena could be predicted accurately in less time.

Although the FEA is a powerful tool, it might sometimes require high computational power, depending on the problem. The number of numerical simulations and ballistic experiments can be reduced by creating an Artificial Neural Network (ANN). The neural network uses statistical non-linear regression-based calculation, and it is one of the most robust techniques in computer science. The method has been used in many fields other than engineering to simulate complex systems. The power of an ANN solution comes from the learning capability of the computer. The neural network system inspired by the human brain system which can imitate the way that humans learn, and after the end of the training, similar problems can be solved without the need for any preparation of the system set up for a similar system. In this section, a literature review of ballistic impact simulations and artificial neural network researches is given. An investigation was conducted by Arndt et al. [15] to combine the FE method with a neural network for a groundwater engineering problem. Numerous numbers

of experiments and FE analyses were performed, and results were used for the ANN training.

Chan et al. [16] are studied a similar integration of the FEM and the ANN for metal-formed product design. Examining the essential design parameters for metal forming applications, evaluation of design performance is done with FE simulations. The metal forming application contains a large number of parameters which are tooling design, material properties selection, metal formed part design, etc. Therefore, doing the parameter sensitivity analysis for each design parameter by FE simulations is a very time-consuming task to find the optimal design. In this study, the design parameters which are geometric parameters of the punch, are used as input parameters. The effective stress on punch and the maximum punch load to make forming applications are taken as an output parameters for FE simulations. A sufficient amount of analyses were performed and results were used to create the ANN setup. The optimum design prediction time is reduced by about 60% with the help of ANN training.

Additionally, Shabani et al. [17] used ANN to find mechanical properties of Al-Si(356) material which are the yield strength, the ultimate tensile strength, and elongation percentage for the solidification process. Experiments and FE simulations were performed for the solidification of A356 alloy. Simulations were performed to create input data for the cooling rate and the temperature gradient. The ANN tool was used to predict the material yield strength, the elongation percentage, and the ultimate tensile strength. Also, Haghdadi et al. [18] worked on the A356 aluminum alloy to predict the material behavior under various thermomechanical conditions by using the ANN and the FE method. Results showed that the ANN tool is such a robust tool to predict the flow behavior of cast A356 material.

Furthermore, Hambli [19] developed a procedure for the simulation of trabecular bone adaptation process with a FE model and ANN model. The FE model was prepared at the macroscopic level, and neural network training was used for mesoscale predictions. Applied stress and boundary conditions were taken as input parameter for the neural network setup and the averaged bone properties are taken as output. Results of the FE-ANN method found beneficial because remodeling of bones is time-consuming. Gudur et al. [20] also studied the ANN in combination with the FEM. In

this study, the computational time of cold flat rolling simulation was decreased with the help of the ANN. Input data of the problem was taken from both experiments and FE solutions. Artificial neural network-assisted FEM provides a good agreement with reduced computational time and therefore is appropriate for on-line control or optimization. Haj-Ali et al. [21] used ANN to define the constitutive behavior of materials from nanoindentation tests. The load indentation tests were only conducted for the monotonic loading scenario to build the ANN model. Nanoindentation tests were performed on a silicon (Si) substrate with and without a nanocrystalline copper (Cu) film. Inverse neural network (back-calculate) run was trained for material parameters for different copper materials. Comparison with literature showed close results with the FE-ANN approach. In light of the studies mentioned above, the FE-ANN approaches can significantly reduce the simulation times.

1.8 Aim of this study

The determination of the ballistic performance of a vehicle armor is based on several parameters such as the armor thickness and the strike velocity. The FEM is a powerful tool to determine ballistic characteristics; however, the FE simulations of all armor and strikes velocity combinations would be computationally costly. To avoid this, a promising approach is to combine the FEM and ANN to predict the ballistic limit of different armor configurations. Creating a well trained ANN with a sufficient amount of numerical analyses can save computational power and time drastically. This work aims to perceive whether the outcome from a ballistic impact can be predicted with the help of material testing, FE simulations, and Artificial Neural Network (ANN). Experimental and numerical studies were conducted to determine the impact response of high strength aluminum armor at level four protection level of STANAG 4569 [3] standard. A high-speed camera was used for calculations of the residual projectile velocities and projectile output images. An artificial neural network was trained using the tests and numerical results to create a simple ballistic limit tool.

CHAPTER 2

NUMERICAL MODELLING

High-velocity impact problems are highly non-linear problems, which include non-linear material behavior, contact nonlinearity, large deformation of collided parts and nonlinear boundary conditions. Creating a numerical model for a high-velocity impact case requires several parameters to simulate the real impact process in a computer environment. These parameters are mostly related to the material model, the equation of state and the failure model employed. In Figure 2.1 an overview of key ingredients that govern computational ballistics are given. The details of numerical models and numerical formulation are given in Chapter 3.

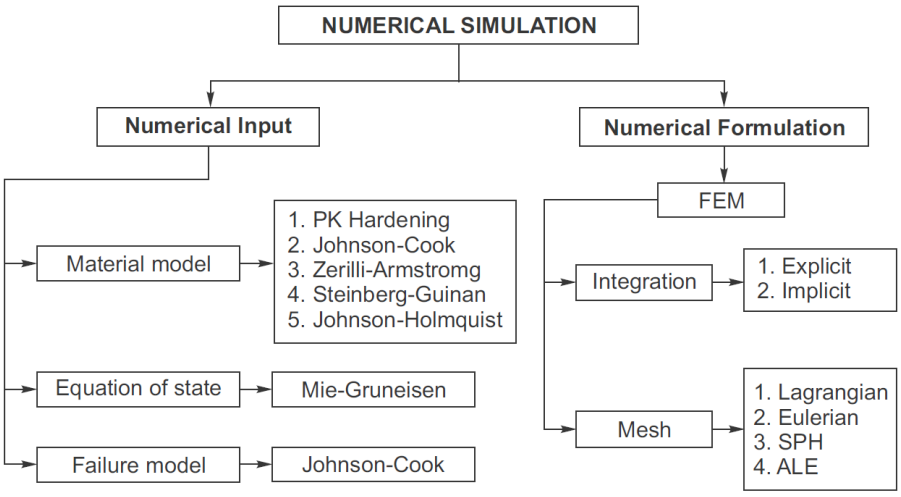

Figure 2.1: Numerical inputs and formulations governing computational ballistics [1].

The FEA starts with Computer-Aided Design (CAD) software. Firstly, projectile and target solid geometry models are generated using relevant design tools. Secondly, a mesh is generated for the solution domain. Thirdly, a suitable material model (details

are given in Chapter 3) is employed and boundary conditions are defined. Then, the solution process can be initialized. During the solution stage, the conservation equations of mass, momentum, energy and entropy are solved. All the material model, damage model and equation of states are integrated into the formulations and these equations are solved for each time-step for each element in the domain. Finally, when the case is solved for a sufficient time, using any post-processing tool, the results (such as strain, stress, velocity, etc.) can be evaluated and visualized. In this study, LSDYNA® is used for the solution phase and LS-Prepost is utilized as a post-processing tool.

2.1 Numerical modeling approaches

Various approaches are used for computational ballistic analyses. The most commonly used approaches are the Lagrangian approach, the Eulerian approach, the Arbitrary Lagrange Euler (ALE) approach and the Smooth Particle Hydrodynamics. In this section, these approaches are briefly explained.

2.1.1 Lagrangian approach

When the Lagrangian solver is used, grid points are fixed on the body, which is analyzed. The Lagrangian solver, therefore, calculates the motion of elements of constant mass [19]. As the body deforms, the grid points move together with the material and the finite elements distort. Figure 2.2 and 2.3 shows the initial mesh and the deformed Lagrangian mesh.

For the problems with small deformations, the Lagrangian approach gives very accurate results because all the material points are tracked. Therefore, mass conservation is precisely satisfied. Compared to other approaches (Eulerian and ALE), the Lagrangian approach requires fewer computational calculations per cycle. Therefore, it is computationally cheaper. However, when extensive deformations occur in FE analysis, elements can be highly distorted during the deformation process. Highly

distorted elements reduce the accuracy on one side and require smaller time increments that result in higher computational cost on the other side. In order to prevent this problem, the material failure definition and the material model, which are employed in FE analysis, must be chosen carefully. With the help of accurate material failure modeling, unrealistic solutions and small times steps can be prevented within the Lagrangian approach.

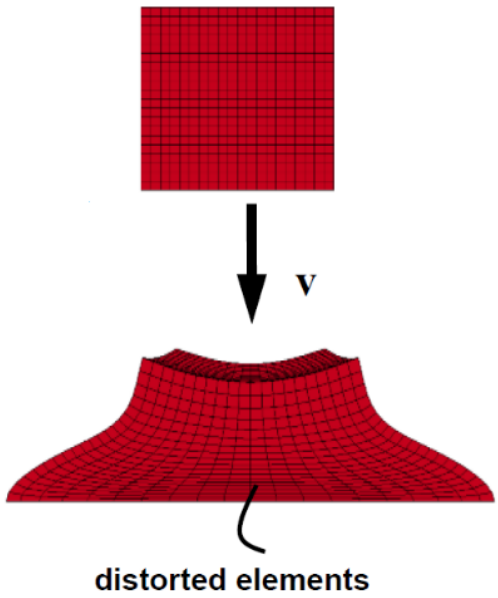

Figure 2.2: Deformed lagrangian elements [6].

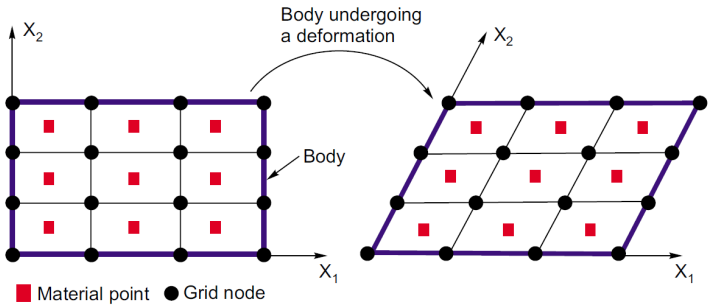

Figure 2.3: Lagrangian mesh and modeling [1].

2.1.2 Eulerian approach

The Eulerian approach is used mostly for fluid-like material behavior modeling under very large deformations. For example, the bullet and armor materials undergo such deformations that the material can reach the melting point, which makes the Eulerian formulation very suitable. The essential advantage of this approach is that the arbitrary material motion is permitted.

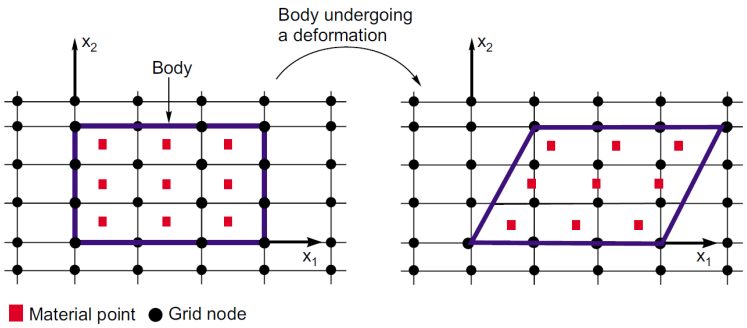

Figure 2.4: Eulerian mesh [1].

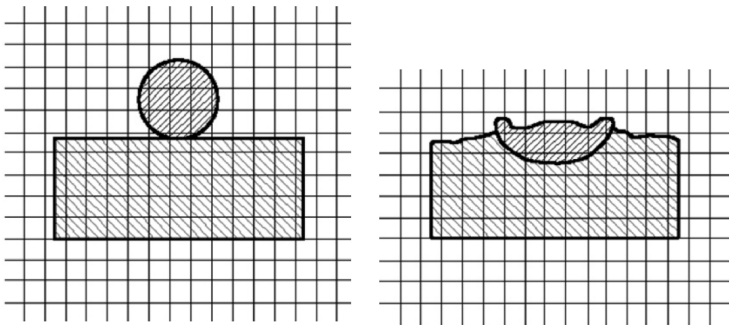

Figure 2.5: Eulerian mesh [2].

In Figure 2.4 and Figure 2.5 an Eulerian domain is illustrated. In Figure 2.5 grid points remain stationary in space during the simulation. Material flows from one element to the other throughout the mesh, where the mass is conserved. The distortion of the element is prevented by transferring material through the mesh domain. Therefore the Eulerian approach is suitable for problems which involve very large deformations. As given in Figure 2.5, the projectile and target flow do not distort the Eulerian mesh

while the deformation of material can still be observed.

The Eulerian approach is computationally expensive compared to the Lagrangian approach. The computational cost difference between these two approaches comes from the material transfer from one element to another and recording the element data for each material that exists within the Eulerian approach. Every element can contain one to many different materials, and the location of each material needs to be traced. Additionally, tracking material transfer interfaces, plasticity, and failure modeling are difficult tasks in the Eulerian approach.

2.1.3 Arbitrary Lagrange Euler coupling

The Arbitrary Lagrange Euler (ALE) approach is a hybrid method which combines the Lagrangian formulation with the Eulerian approach. Mine blast simulations, sloshing analysis and other fluid-structure interaction problems are commonly modeled with the ALE approach. The ALE method can be explained by the help of Figure 2.6.

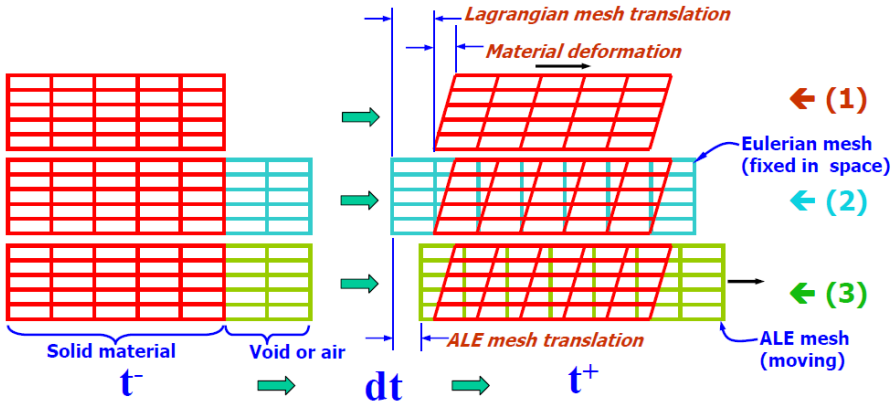

Figure 2.6: Difference between Lagrangian, Eulerian and ALE [6].

In Figure 2.6 overlapping meshes are given. One is a background mesh which can move arbitrarily in space (i.e., a Lagrangian Mesh), and the other is attached to the material which "flows" through the former moving mesh. This can be visualized in two steps. First, the material is deformed in a Lagrangian step just like the Lagrangian

formulation. Then, the element state variables in the "Lagrangian elements" (red) are remapped or advected or distributed back onto the moving (background) reference ALE mesh (green). The main difference between the pure Eulerian approach versus the ALE method is different amounts of material being advected through the meshes due to the reference mesh positions [6].

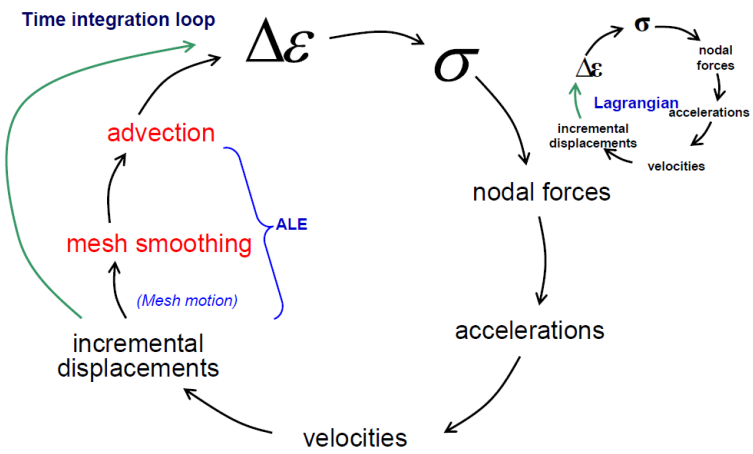

Figure 2.7: Time integration loop of ALE approach [6].

In Figure 2.7 time integration loop of the ALE method is shown. Firstly, Lagrangian time derivatives of displacement are calculated, and the acceleration and velocity history variables are updated. Afterward, the relative motion between the mesh and the material is computed and the acceleration and velocity history variables are updated once again. Compared with the Lagrangian approach, all of these calculations are done a minimum twice as much. After the Lagrangian step, the ALE element calculation loop is started.

2.1.4 Smooth Particle Hydrodynamics

The Smooth Particle Hydrodynamics (SPH) represents a mesh-free solution which can also be used for cases that involve large deformations. In the SPH numerical discretization of the continuum is achieved with a set of nodes without the node to node connecting mesh. Comparison of a Lagrange mesh and SPH model is shown in Figure 2.8. Within the SPH formulation, the particles are free movable points with

a fixed mass, and they all have coherence only through an interpolation function. The kernel estimate allows us to describe the conservation of mass, momentum, and energy in terms of interpolation sums [22]. The disadvantage of the SPH approach is its limited accuracy in modeling high energy events. Moreover, the calculation of contact forces between SPH particles is problematic. Due to the high oscillations of interface forces between SPH particles low-level accuracy results can be obtained.

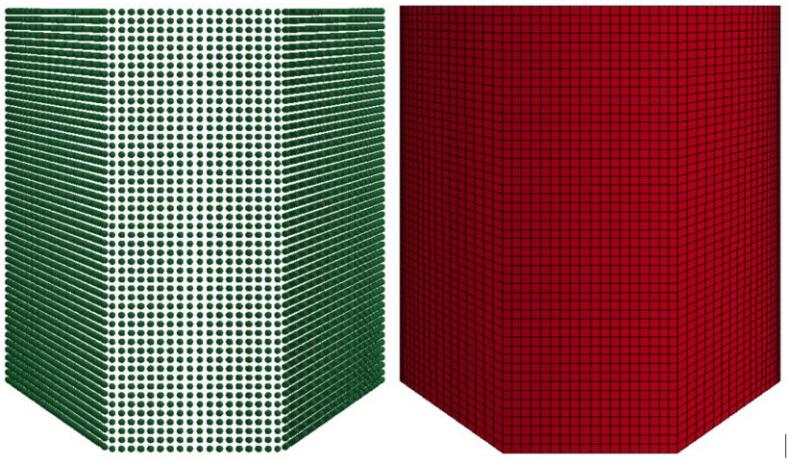

Figure 2.8: SPH (left) and Lagrange (right) representation of Fragment Simulating Projectile

2.2 Integration methods

There are two types of integration methods used in numerical simulations:

1. Implicit time integration

2. Explicit time integration

The implicit time integration is widely used in simulations that involve low strain rates (less than ($10^2 \mathrm{s}^{-1}$) and low-velocity values. However, the implicit time integration provides unconditional numerical stability for the solution. Impact problems must be examined in detail for the selection of the type of solver. The equation of motion (2.1)

is used for both integration methods to advance in time.

$$\mathrm{M\ddot{u}} + \mathrm{C\dot{u}} + \mathrm{Ku} = \mathrm{F(t)} \tag{2.1}$$

On the left side of (2.1), M represents the mass matrix, C is the damping coefficient matrix, and K is the stiffness matrix. Nodal displacement vectors are given with u. Therefore, $\dot{\mathrm{u}}$ and $\ddot{\mathrm{u}}$ are the nodal velocity and nodal acceleration vectors. On the right side of the (2.1), F(t) is the external nodal forces. At any point in time, (2.1) is solved for nodal accelerations from nodal displacements, velocities and external forces respectively.

Explicit time marching method is frequently used for any impact problems. Implementation of an explicit finite element code is quite easy and requires low memory storage. However, explicit integration is conditionally stable, which is its major disadvantage. To explain it further, there is a restriction for time step value, which cannot be exceeded during the solution process. The critical time step ($\Delta \mathrm{t_{cr}}$) value is controlled by the size of the smallest element in the FE model, and the largest natural frequency of model. The critical time step is found as shown in (2.2).

$$\Delta \mathrm{t} = \frac{\ell_{\mathrm{s}}}{\mathrm{c}} = \ell_{\mathrm{s}}\sqrt{\frac{\rho}{\mathrm{E}}} \leq \Delta \mathrm{t_{cr}} = \frac{2}{\mathrm{w_{max}}} \tag{2.2}$$

In (2.2), ℓ_{s} represents the minimum edge length of the element, ρ represents the density, $\mathrm{w_{max}}$ is the highest eigenfrequency of the system and E represents Young's modulus of the material. Based on the principle that time step is proportional to the square root of mass density (sound speed inversely proportional to the square root of mass), an increase in mass density (or adding element mass) will increase element time step and thereby reduce the computational time. Robustness of the explicit time integration is hinged upon to the value of the critical time-step of the FE model [23].

2.2.1 Implicit integration

Within the implicit integration method, equations of motion are evaluated at $t + \Delta t$ time. However, the nodal accelerations and displacements at $t + \Delta t$ are unknown. Expanding the Taylor series for displacement equation at third order:

$$u_{t+\Delta t} = u_t + \Delta t \dot{u}_t + \frac{\Delta t^2 \ddot{u}_t}{2} + \beta_t \Delta t^3 \dddot{u}_{t+\Delta t} \tag{2.3}$$

$$\dot{u}_{t+\Delta t} = \dot{u}_t + \Delta t \ddot{u}_t + \gamma_T \frac{\Delta t^2}{2} \dddot{u}_{t+\Delta t} \tag{2.4}$$

where β_t and γ_T are constants for Taylor series expansion and Δt is the time step size. To be able to determine the third order derivative of displacement at time $t + \Delta t$, a linear change of acceleration assumption at a given time step is made:

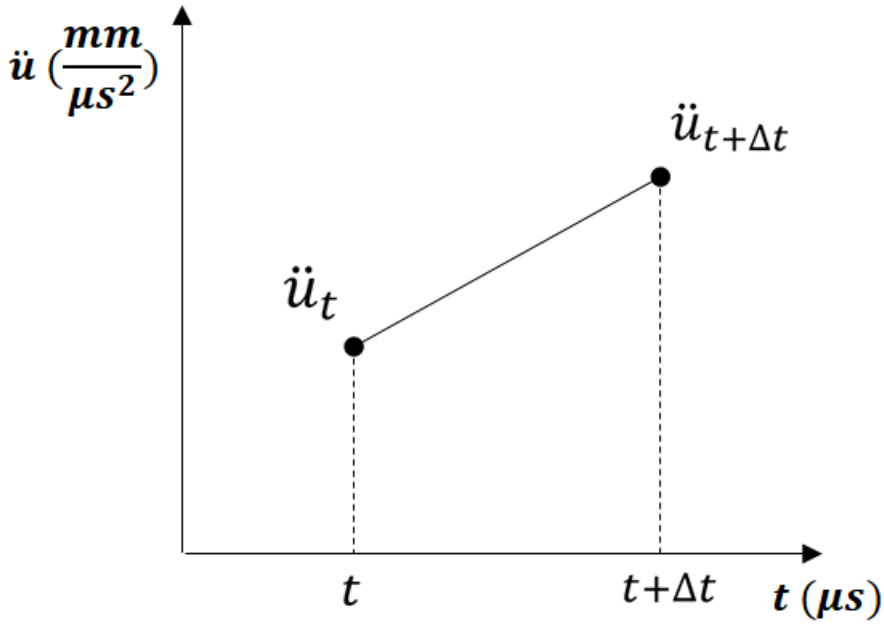

Figure 2.9: The linear assumption for acceleration

$$\dddot{u}_{t+\Delta t} = \frac{\ddot{u}_{t+\Delta t} - \ddot{u}_t}{\Delta t} \tag{2.5}$$

Using (2.5) in both Eqs. (2.3) and (2.4) will give the Newmark's solution for the

$u_{t+\Delta t}$ and $\dot{u}_{t+\Delta t}$ at time $t + \Delta t$:

$$u_{t+\Delta t} = u_t + \Delta t \dot{u}_t + \frac{\Delta t^2}{2}\left(1 - 2\beta_T\right)\ddot{u}_t + \beta_T \Delta t^2 \ddot{u}_{t+\Delta t} = u_t^* + \beta_T \Delta t^2 \ddot{u}_{t+\Delta t} \quad (2.6)$$

$$\dot{u}_{t+\Delta t} = \dot{u}_t + \left(1 - \gamma_T\right)\Delta t \ddot{u}_t + \gamma_T \Delta t \ddot{u}_{t+\Delta t} = \dot{u}_t^* + \gamma_T \Delta t \ddot{u}_{t+\Delta t} \quad (2.7)$$

where u_t^* and $\dot{u}_t^*$ used for a compact representation. Setting the β_T and γ_T constants zero, changes the Eqs. (2.6) and (2.7) into an explicit form. Evaluation of the displacement and the velocity dependent only on one unknown at time t Eqs. (2.6) and (2.7) unconditionally stable. Hughes and Taylor [24] have proven that this integration method is unconditionally stable if $2\beta_T \geq \gamma_T \geq 1/2$ and conditionally stable if $\gamma_T \geq 1/2$ and $\beta_T \leq (1/2)\gamma_T$. Usually, these constants are chosen as $\beta_T = 1/4$ and $\gamma_T = 1/2$, which is known as the average acceleration method [24]. Using these constants values in Eqs.(2.6) and (2.7) and insertion of (2.6) and (2.7) into (2.1) give:

$$\left[M + \frac{1}{2}C\Delta t + \frac{1}{4}K\Delta t^2\right]\ddot{u}_{t+\Delta t} = F^{ext}_{\ddot{u}_{t+\Delta t}} - Cu_t^* - Ku_t^* \quad (2.8)$$

Rewriting (2.8) gives:

$$M^*\ddot{u}_{t+\Delta t} = F^{ext}_{\ddot{u}_{t+\Delta t}} - F^* = F^{residual}_{t+\Delta t} \quad (2.9)$$

where $F^* = Cu_t^* + Ku_t^*$ and $F^{residual}_{t+\Delta t}$ is the subtraction of the forces seen in (2.9). The nodal acceleration values are found by solving the equation set with the Newton-Raphson iteration method. After the calculation of nodal accelerations, nodal velocities and displacements are found from (2.6). This solution process is repeatedly done for each node for every time step until the solution terminates [24].

2.2.2 Explicit integration

The explicit integration solution uses the central difference method for most applications. Nodal accelerations at $t + \Delta t$ are predicted at t time from (2.1). Nodal acceler-

ation is assumed to be constant during the time step, and its value is calculated from the initial state of equilibrium. Therefore, the time step must be sufficiently small, considering the linear change of acceleration (see implicit methods). Calculation of the acceleration is given in (2.10):

$$\ddot{u}_{t+\Delta t} = M^{-1} F_t^{residual} \tag{2.10}$$

Using the central difference method displacements and velocities are calculated as follows:

$$\dot{u}_{t+\Delta t} = \dot{u}_t + \Delta t \ddot{u} \tag{2.11}$$

$$u_{t+\Delta t} = u_t + \Delta t \dot{u}_{t+\Delta t} \tag{2.12}$$

The explicit integration method is only stable if the time step is smaller than the so-called critical time step (conditionally stable). The critical time step is related to the highest eigenfrequency of the system and the mesh size of the model. Generally, the time-steps for explicit codes are 100-1000 times smaller than implicit codes. However, since the values at the next time step are computed directly, the cost of each time increment is relatively low. Explicit methods have a greater advantage over implicit methods if the time step of the implicit solution has to be small, and if the model size is large [22].

2.3 CONCEPTS IN NUMERICAL SIMULATION

In this chapter, simulation concepts such as hourglass deformation and contact definition methods are discussed.

2.3.1 Hourglass Deformation and Hourglass Damping

Hourglass deformation is a mesh-based problem which generally occurs in impact simulations employing a Lagrangian approach. Even though the hourglass deformation is not the primary problem, it has to be handled in order to reduce the unrealistic behavior of collided parts.

2.3.1.1 Hourglass Deformation

The source of the hourglass problem emerges from the reduced integration (one integration point). One integration point element may produce zero energy deformation modes (hourglass mode) in Lagrangian elements.

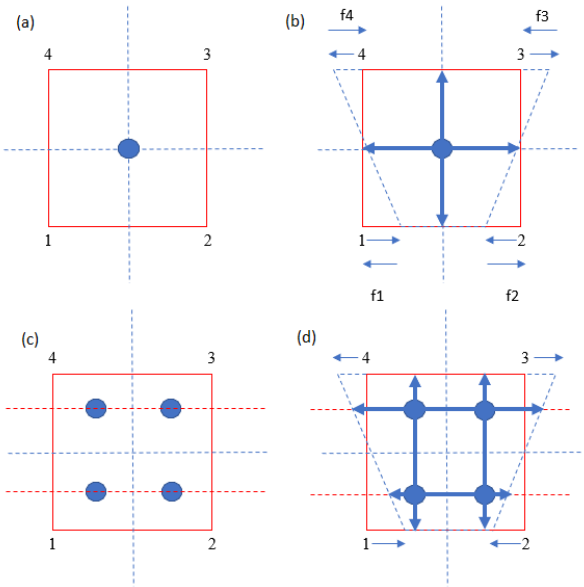

Figure 2.10: (a) An undeformed and deformed (b) one-point integration element, (c) an undeformed and deformed (d) full integration element

The hourglass mode is a deformation mode that produces zero strain at all integration points. Figure 2.10 shows a comparison between one point integration element and a fully integrated element and their deformation characteristics. Blue points represent the integration points, and 1,2,3,4 are the node numbers of the element. f1, f2, f3, and f4 are hourglass penalty forces. In Figure 2.10 (a) and (b), one point integration

element and its deformation are shown schematically. As it is shown in Figure 2.10 (a) during the deformation of a one point integration element, no strain is generated at the integration point. If the integration point (Gauss point) senses no strain under a certain deformation mode, the resulting element stiffness matrix will have no resistant to that deformation mode. Therefore, the element shows a very soft response to this deformation mode. On the other hand, the strains at integration points, are not zero for a fully integrated element because the change of length can be taken into account over integration points as seen in Figure 2.10 (c)-(d).

2.3.1.2 Hourglass Damping

A penalty stiffness is predefined by the user in order to prevent the hourglass modes. Consider the one integration point element in Figure 2.10 again. One needs to introduce a nodal force field that opposes the hourglass component of nodal velocities. These forces must thus be opposed to the hourglass base vector. Viscous hourglass forces are defined as

$$\begin{bmatrix} f_1 \\ f_2 \\ f_3 \\ f_4 \end{bmatrix} = \mathrm{h_m a \dot{u}_{hx}} \begin{bmatrix} 1 \\ -1 \\ 1 \\ -1 \end{bmatrix} \tag{2.13}$$

$$\mathrm{a} = \frac{\mathrm{c}\rho}{4}(\mathrm{tA})^{\frac{2}{3}} \tag{2.14}$$

where $\mathrm{h_m}$ is a dimensionless user-defined penalty factor (default value is 0.1), $\dot{\mathrm{u}}_{\mathrm{hx}}$ is the nodal velocities and a has the dimension of viscosity (Ns/m) and given as (2.14). In (2.14) A represents the area of the element and t is time. Using (2.13) a viscous hourglass damping force field is generated.

Alternatively, stiffness hourglass forces can be used which are defined as follows:

$$\begin{bmatrix} f_1 \\ f_2 \\ f_3 \\ f_4 \end{bmatrix} = \mathrm{h_m} \int \frac{\mathrm{Et}}{8} \dot{\mathrm{u}}_{\mathrm{hx}} \begin{bmatrix} 1 \\ -1 \\ 1 \\ -1 \end{bmatrix} dt \tag{2.15}$$

In (2.15) stiffness based hourglass damping formulation is shown. E represents Young's modulus of the element and t represents the time. The viscous hour glassing only stops the hourglass mode from being further developed. On other the hand, the stiffness hourglass damping forces push the element back towards its undeformed configuration. The stiffness based hourglass considerably stiffens the behavior of the solid elements. Since the hourglass forces cannot be expected to compensate exactly the missing element stiffness, an accurate result requires low hourglass energy compared to deformation energy. Ideally, the hourglass energy should be less than ten percent of the internal energy.

2.3.2 Contact-Impact Methods

Modeling the interaction between the impactor and the target is another essential point of numerical modeling. Using implicit codes, nonlinear contact modeling is a very challenging task. On the other hand, explicit codes are so powerful and useful for nonlinear contact problems.

Considering explicit codes, there are three distinct methods for defining contacts:

1. the kinematic constraint method
2. the penalty method
3. the distributed parameter method

On the contact interface, one side of the contact is named as the slave surface, and another side is called the master surface. The selection of the master surface and the

slave surface is arbitrary in case of modeling symmetric contact. In other cases, there are several rules of thumbs to determine master and slave surfaces (for details see 2.3.2.1). Since the most commonly used contact definitions are the kinematic constraint method and the penalty method, below, only these methods will be discussed.

2.3.2.1 Kinematic Constraint Method

The kinematic constraint method is also known as the nodal constraint method. In this method, the degree of freedom constraints is imposed on the global equations by a transformation of the nodal displacement components of the slave nodes along with the contact interface [7]. The transformation eliminates normal degrees of freedom of slave nodes. Additionally, normal forces are distributed from slave nodes to master nodes during this transformation process.

In Figure 2.11, two surfaces, one master and one slave (x nodes belong to the master surface) with different sizes of meshes, are illustrated. The slave surface has a coarser mesh compared to the master surface. As a result of this, nodes of the master surface can easily penetrate the slave surface without any resistance. This penetration can lead hourglassing to elements in contact and reduce the accuracy of the model. Therefore, the slave contact surface should have a finer mesh to the master side.

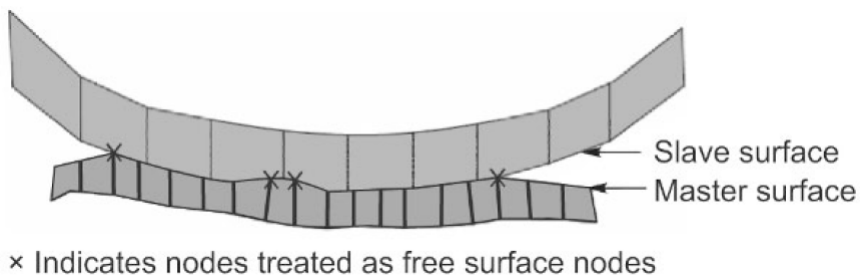

Figure 2.11: Kinematic constraint method [7]

2.3.2.2 Penalty Method

This method is based on inserting an elastic compression-only spring in the normal direction between the penetrating element nodes and the contact surfaces. The spring force is calculated from the thickness and bulk modulus of the element for each slave and master segment. Three types of penalty algorithms are used, which are:

1. **The standard penalty formulation** is employed when the parts in contact have similar stiffness values.
2. **The soft constraint penalty formulation** is widely used whenever there are significant differences of stiffness, density, mechanical properties between parts in contact.
3. **The segment-based penalty formulation** uses a slave-master segment approach different from the classical slave node-master segment approach.

In this work, standard penalty formulation is employed for contact interactions.

CHAPTER 3

MATERIAL MODELLING AND FAILURE MODELS

Selection of the right material model and determination of the real material constants from experiments are the most challenging parts of FE simulations. LSDYNA® software includes two hundred material models. For ballistic problems, suitable material models are explained in this chapter. Additionally, the most commonly used theoretical failure criteria and failure models are explained

3.1 Gruneisen parameter

Mie-Gruneisen equation of state comes from statistical mechanics which considers energies of atoms. The equation state (EOS) is a function of pressure p, density ρ, and internal energy e of the material, and it defines the volumetric response (or hydrostatic response) of a material. The Gruneisen parameter can be regarded as the change in pressure through an increase of specific internal energy at constant volume [25].

The Gruneisen parameter is commonly represented with Γ symbol, and the definition is:

$$\Gamma = \frac{1}{\rho}\left(\frac{\delta \mathrm{p}}{\delta \mathrm{e}}\right)_{\mathrm{v}} \tag{3.1}$$

To evaluate the Gruneisen parameter in measurable properties, $\left(\frac{\delta \mathrm{p}}{\delta \mathrm{e}}\right)_{\mathrm{v}}$ can rewritten

as:

$$\left(\frac{\delta \mathrm{p}}{\delta \mathrm{e}}\right)_{\mathrm{v}} = \frac{\left(\frac{\delta \mathrm{p}}{\delta \mathrm{T}}\right)_{\mathrm{v}}}{\left(\frac{\delta \mathrm{e}}{\delta \mathrm{T}}\right)_{\mathrm{v}}} \tag{3.2}$$

where $\left(\frac{\delta \mathrm{e}}{\delta \mathrm{T}}\right)_{\mathrm{v}} = \mathrm{C_V}$ is the specific heat per unit mass. The term $\left(\frac{\delta \mathrm{p}}{\delta \mathrm{T}}\right)_{\mathrm{v}}$ can be derived using the Maxwell's relation [26]

$$\left(\frac{\delta \mathrm{p}}{\delta \mathrm{T}}\right)_{\mathrm{v}} = \left(\frac{\delta \mathrm{p}}{\delta \mathrm{V}}\right)_{\mathrm{T}} \left(\frac{\delta \mathrm{V}}{\delta \mathrm{T}}\right)_{\mathrm{p}} \tag{3.3}$$

where $\left(\frac{\delta \mathrm{p}}{\delta \mathrm{V}}\right)_{\mathrm{T}} = \mathrm{K_T}$ is the isothermal bulk modulus and $\left(\frac{\delta \mathrm{V}}{\delta \mathrm{T}}\right)_{\mathrm{p}} = \beta$ is the coefficient of the volumetric expansion. In the case of an isotropic solid element, volumetric expansion can be used as proportional to linear thermal expansion, α as $\beta = 3\alpha$. Insertion of the parameters $\mathrm{C_V}, \alpha, \mathrm{K_T}$ in Eq.(3.2) gives:

$$\left(\frac{\delta \mathrm{p}}{\delta \mathrm{e}}\right)_{\mathrm{v}} = \frac{3\alpha \mathrm{K_T}}{\mathrm{C_V}} \tag{3.4}$$

Then using (3.4) and (3.3) a physically measurable Gruneisen parameter is obtained as

$$\Gamma = \frac{3\alpha \mathrm{K_T}}{\rho \mathrm{C_V}} \tag{3.5}$$

The Gruneisen parameter is taken as $\Gamma = 2.0$ for most ambient conditions. Furthermore, Γ is assumed to be temperature independent and, $\Gamma\rho$ is taken as a constant for a given solid material for a wide pressure range [27].

3.1.1 Shock Rankine-Hugoniot conditions and relation

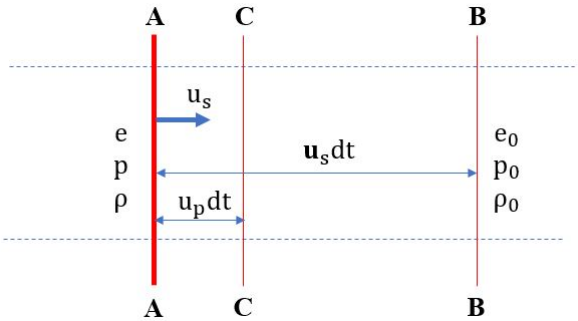

Figure 3.1: Schematic view of a shock front (line C) propagating through a compressible material [8].

The Rankine-Hugoniot equations involve the conservation of mass, momentum, and energy equations which are shown in Eqs. (3.6), (3.7) and (3.8).

$$\rho_0 \mathrm{u_s} = \rho \left(\mathrm{u_s} - \mathrm{u_p}\right) \tag{3.6}$$

Over time increment dt change of momentum can be written as $\rho_0 \mathrm{u_s dt u_p}$, and pressure impulse is $\mathrm{p} - \mathrm{p_0 dt}$. Therefore, the conservation of momentum can be written as

$$\mathrm{p} - \mathrm{p_0} = \rho_0 \mathrm{u_s u_p} \tag{3.7}$$

In (3.7) $\rho_0 \mathrm{u_s}$, is known as the shock impedance.

After time increment dt the kinetic energy of the plate is $\frac{1}{2}\rho_0 \mathrm{u_s dt u_p^2}$, the change in the internal energy is $\rho_0 \mathrm{u_s dt(e - e_0)}$, and the work done by the pressure is $\mathrm{pu_p}$ dt. Therefore, the conservation of energy can be written as

$$\frac{1}{2}\rho_0 \mathrm{u_s dt u_p^2} + \rho_0 \mathrm{u_s dt(e - e_0)} = \mathrm{pu_p dt} \tag{3.8}$$

A detailed version of the derivation of these equations is given in Zukas et al. [3].

Excluding $\mathrm{u_s}$ and u from (3.8) gives Rankine-Hugoniot relation as:

$$(\mathrm{e} - \mathrm{e_0}) = \frac{1}{2}(\mathrm{p} + \mathrm{p_0})\,(\mathrm{v_0} + \mathrm{v}) \tag{3.9}$$

where $\frac{1}{\rho_0} = \nu_0$ and $\frac{1}{\rho_1} = \nu_1$ represent the uncompressed and the compressed specific volumes, respectively. Equations (3.6) - (3.9) are generally referred to as jump conditions. These conditions should always be satisfied at the shock front for all impact applications.

3.1.2 Mie-Gruneisen equation of state

The Mie-Gruneisen equation of state (EOS) comes from statistical mechanics and can be expressed with the Gruneisen parameter given in (3.5):

$$\delta \mathrm{p} = \Gamma\rho\delta\mathrm{e} \tag{3.10}$$

where $\Gamma\rho$ is taken as a material constant as already mentioned before in Section 3.1

The difference in the internal energy is proportional to the difference in pressure at 0K. One can write (3.10) as:

$$(\mathrm{p} - \mathrm{p_{ref}}) = \Gamma\rho(\mathrm{e} - \mathrm{e_{ref}}) \tag{3.11}$$

This reference state can easily be rewritten in other forms. The most common known form of the Mie-Gruneisen is given in [28], [29], [30]. The full description of the Mie-Gruneisen EOS comes from Hugoniot pressure and energy equations which can be found in [7] in detail.

3.2 Plasticity

High-velocity impact problems generally include large deformation of both the impactor and the target. Therefore, the impact process is dominated by plasticity. For the low-velocity impact cases, target and impactor are first deformed elastically, and

then they return to their original state. If the distortion is too significant, the projectile and the target will exceed their elastic limits and deform plastically. Whether plastic deformations occur or not is generally controlled by the von Mises yield criterion which is given in (3.12)

$$\mathrm{F} = \sigma_{\mathrm{eq}}^2 - \sigma_{\mathrm{y}}^2 \tag{3.12}$$

In (3.12) F is the yield function of the material and σ_{y} is the yield stress. The von Mises stress, σ_{eq}, is given by:

$$\sigma_{eq} = \frac{1}{2}\sqrt{(\sigma_1 - \sigma_2)^2 + (\sigma_2 - \sigma_3)^2 + (\sigma_3 - \sigma_1)^2} \tag{3.13}$$

where $\sigma_1, \sigma_2, \sigma_3$ represent the principal stresses. The restrictions proposed by Kuhn-Tucker rule, which are shown in Eqs. (3.14) and (3.15), indicate whether the stress is inside or on the yield surface.

$$(\mathrm{F} < 0) \vee (\mathrm{F} = 0 \wedge \dot{\mathrm{F}} < 0), \mathrm{Elastic} \tag{3.14}$$

$$(\mathrm{F} = 0 \wedge \dot{\mathrm{F}} = 0), \mathrm{Elastic} - \mathrm{Plastic} \tag{3.15}$$

Generally, for metals with elastic-perfectly plastic behavior, yielding characteristics are determined by using the Von-Mises criterion. The von-Mises criterion is suitable for high strength materials, such as armor steels and the high strength aluminum alloys [27]. The collision causes large deformations in both the projectile and the target. Additionally, for materials which go through the large deformation in high-velocity impact events, the progress is an adiabatic process. During the deformation process for impact scenarios, temperatures can reach 200-500°C, which is around the melting point of few metals, as given in [1]. The temperature directly affects the thermal softening/hardening behavior of the materials. Therefore, the effect of the strain rate and the thermal effects must be included for high-velocity impact problems.

There are many material models for the high-velocity impact behavior of metals such as the kinematic hardening model, the thermo elastic-plastic material model, the power-law isotropic material model, Johnson-Cook material model, the Zerilli-Armstrong material model, and the Steinberg-Guinan model. In this study, the Johnson-Cook material model is employed both for the projectile and the target. Therefore, only the Johnson-Cook material model will be explained in the next sections.

3.2.1 Johnson-Cook Model

The Johnson-Cook model was introduced in 1983. It is an empirical material model, which is prepared by a sufficient amount of test data at different strain rates and temperatures. This is the appropriate model for problems, including high strain rate range and extensive temperature changes. For each phenomenon (strain hardening, strain rate hardening, and thermal softening), an independent term is created. By multiplying these terms, the flow stress is defined as a function of the effective plastic strain, strain rate, and temperature [1]. The constitutive relation of the Johson-Cook model is shown in (3.16).

$$\sigma_{\mathrm{y}} = \left[\mathrm{A} + \mathrm{B}\varepsilon_{\mathrm{p}}^{\mathrm{n}}\right]\left[1 + \mathrm{C}\ln\left(\dot{\varepsilon}^{*}\right)\right]\left[1 - \left(\mathrm{T}^{*}\right)^{\mathrm{m}}\right] \tag{3.16}$$

with

$$\mathrm{T}^{*} = \frac{\mathrm{T} - \mathrm{T}_{\mathrm{ref}}}{\mathrm{T}_{\mathrm{m}} - \mathrm{T}_{\mathrm{ref}}} \quad \text{, and,} \quad \dot{\varepsilon}^{*} = \frac{\dot{\varepsilon}_{\mathrm{p}}}{\dot{\varepsilon}_{0}} \tag{3.17}$$

where *A* is the yield stress, *B* is the strain hardening coefficient, *n* is the strain hardening exponent, ε_{p} is the effective plastic strain, ($\dot{\varepsilon}_{\mathrm{p}}$) is the effective plastic strain rate, $\dot{\varepsilon}_{0}$ is the reference strain rate used in quasi-static tensile tests, $\dot{\varepsilon}^{*}$ is effective plastic strain rate, *C* is the strain rate coefficient, T_{m} is the melting temperature and $\mathrm{T}_{\mathrm{ref}}$ is the reference temperature.

The parameters in J-C model (*n*, *C*, and *m*) are determined from an empirical curve fit of dynamic yield stress. Firstly, the second and third brackets of (3.16) are eliminated to determine *n*. In order to eliminate second bracket, $\dot{\varepsilon}_{\mathrm{p}}$ is chosen as the strain rate of interest (for example maximum strain rate in test data), and $\dot{\varepsilon}_{0}$ is set to the same value of $\dot{\varepsilon}_{\mathrm{p}}$ so that $\dot{\varepsilon}^{*} = 1s^{-1}$. Hence, the second term of the J-C equation is now equal to one. To eliminate the third bracket, $\mathrm{T}_{\mathrm{ref}}$ is set to test temperature which yields to $\mathrm{T}^{*} = 1$. After eliminating the second and the third terms, n can be calculated from the slope of a plot between $\ln(\sigma_{\mathrm{y}} - \mathrm{A})$ vs $\ln(\mathrm{B}\varepsilon_{\mathrm{p}})$. Secondly, to determine C, only the third bracket of (3.16) is eliminated by setting again $\mathrm{T}_{\mathrm{ref}}$ to test temperature. This reduces (3.16) to (3.18):

$$\sigma_{\mathrm{y}} = \left[\mathrm{A} + \mathrm{B}\varepsilon_{\mathrm{p}}^{\mathrm{n}}\right]\left[1 + \mathrm{C}\ln\left(\dot{\varepsilon}^{*}\right)\right] \tag{3.18}$$

From dynamic yield stress for every fixed plastic strain at various strain rates, *C* is the slope of $\ln([\frac{\sigma_{\mathrm{y}}}{(\mathrm{A}+\mathrm{B}\varepsilon_{\mathrm{p}}^{\mathrm{n}})}]-1)$ vs $\ln(\dot{\varepsilon}^{*})$. Thirdly, to determine *m*, only the second term is eliminated. To do this, as already mentioned above, $\dot{\varepsilon}^{*}$ is arranged to $1s^{-1}$. After this elimination (3.16) reduces to (3.19):

$$\sigma_{\mathrm{y}} = \left[\mathrm{A}+\mathrm{B}\varepsilon_{\mathrm{p}}^{\mathrm{n}}\right]\left[1-(\mathrm{T}^{*})^{\mathrm{m}}\right] \tag{3.19}$$

In (3.19) *m* is the slope of the $\ln(1-[\frac{\sigma_{\mathrm{y}}}{(\mathrm{A}+\mathrm{B}\varepsilon_{\mathrm{p}}^{\mathrm{n}})}])$ vs $\ln(\mathrm{T}^{*})$ plot. Finally, the material constants C and m are determined using the least-square method [31].

3.3 Material Failure Modelling

Evaluation of a failure in ballistic problems is a very complicated task. The impact process contains so many complexities like large deformation, high strain rates, high pressures, and high temperatures. All of these phenomena should be taken into account for true material failure. There are two ways to model failure in the numerical environment. The first method is called as *defining a failure criteria*. This option assigns a failure value for specific parameters like maximum effective plastic strain and maximum pressure attained in elements. If the element exceeds the value of the failure limit, it is eroded from the FE model. Therefore, the real failure of the material cannot be modeled with that option because the strain rate effects and the continuum damage mechanisms are eliminated. The second option is named as *failure model*, which accounts for the degradation of the stiffness of the structure after the failure occurs. Therefore, it provides a more realistic behavior of the structure.

Both of above mentioned methods are used in ballistic simulations, but especially for high-velocity impact cases, the use of material failure models is more common. Defining failure criteria could cause unrealistic element erosion for significant deformation/high strain rate problems.

3.3.1 Failure Models

The material model determines the material's strength according to its strain hardening and softening response. The failure and the damage models predict the damage in the material during a collision. The damage of material is estimated by the loss of cohesion in its interior, leading to either its complete disintegration or to some internal damage which is manifested by the appearance of new free surfaces inside the material specimen. Several models are available to predict the material fracture and they are developed based on three broad approaches such as physical, micro-statistical and phenomenological [27]. As damage progresses, discontinuities in the form of microcracks may develop and stress concentration points arise from these discontinuities. Two types of fracture, namely brittle and ductile, occur in the materials.

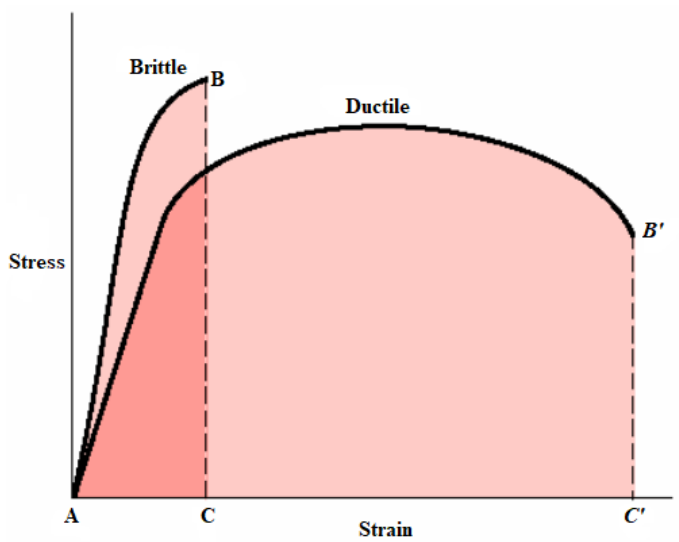

Figure 3.2: Failure types from left to right; brittle, ductile from brittle and ductile, respectively [9].

Brittle fracture is the fracture between atomic bonds under relatively small deformation. When the local strain energy exceeds the energy of the atomic bonds, fracture occurs. In brittle fracture, the crack grows abruptly with a small amount of plastic strain energy. This type of fracture generally occurs on high strength metals with poor ductility and toughness like ceramics, ice, cold metals, etc..

A ductile fracture occurs when materials go through large deformation before frac-

ture. The crack grows very slowly and moves with a high amount of plastic deformation. Therefore, failure modeling depends on the material type and characteristics. The schematic stress-strain curves for brittle and ductile materials are given in Figure 3.2.

The failure definition of a material can be done according to maximum stress or strain or temperature or strain rate, etc. Many of the material models may depend on stress, strain, or a combination of stress and strain. In this work, employed failure models depend on these variables, and if the variable reaches its critical value, then the material fails.

The response of many materials can be grouped into two: the volumetric response (equation of state) and the deviatoric response (strength model). The plastic deformation of metallic materials is generally independent of the hydrostatic stress components. This component is only related to the volumetric change of the material, whereas the deviatoric stress components determine shape changes. On the other hand, when a metallic material deforms plastically, the volume of the material does not change, but its shape. The decomposition of stress state into volumetric and deviatoric parts reads

$$\begin{bmatrix} \sigma_{11} & \sigma_{12} & \sigma_{13} \\ \sigma_{21} & \sigma_{22} & \sigma_{23} \\ \sigma_{31} & \sigma_{32} & \sigma_{33} \end{bmatrix} = \begin{bmatrix} \sigma_m & 0 & 0 \\ 0 & \sigma_m & 0 \\ 0 & 0 & \sigma_m \end{bmatrix} + \begin{bmatrix} S_{11} & S_{12} & S_{13} \\ S_{21} & S_{22} & S_{23} \\ S_{31} & S_{32} & S_{33} \end{bmatrix} \tag{3.20}$$

where

$$\sigma_{\mathrm{m}} = \frac{\sigma_{11} + \sigma_{22} + \sigma_{33}}{3} \tag{3.21}$$

is the mean stress and

$$\begin{bmatrix} S_{11} & S_{12} & S_{13} \\ S_{21} & S_{22} & S_{23} \\ S_{31} & S_{32} & S_{33} \end{bmatrix} = \begin{bmatrix} 1/3(2\sigma_{11} - \sigma_{22} - \sigma_{33}) & \sigma_{12} & \sigma_{13} \\ \sigma_{21} & 1/3(2\sigma_{11} - \sigma_{22} - \sigma_{33}) & \sigma_{23} \\ \sigma_{31} & \sigma_{32} & 1/3(2\sigma_{11} - \sigma_{22} - \sigma_{33}) \end{bmatrix} \tag{3.22}$$

is the deviatoric stress.

3.3.2 Johnson-Cook Failure Model

The Johnson-Cook failure model is considered as a fracture criterion and is appropriate for the explicit solvers. This failure criterion depends on the maximum strain of an element, which is the function of strain rate and temperature. Additionally the stress triaxiality

$$\sigma^* = \frac{\sigma_{\mathrm{m}}}{\sigma_{\mathrm{eq}}} \tag{3.23}$$

is taken into account in this model. The stress triaxiality is an important parameter since the fail tendency of ductile materials is strongly depends on the pressure exerted on them [27]. This failure model contains a damage parameter marked with D and its defined as follows

$$\mathrm{D} = \frac{\varepsilon_{\mathrm{p}}}{\varepsilon_{\mathrm{f}}} \tag{3.24}$$

where

$$\varepsilon_{\mathrm{p}} = \int_0^{\mathrm{t}} \dot{\varepsilon}_{\mathrm{p}} \mathrm{dt} \tag{3.25}$$

$$\dot{\varepsilon}_{\mathrm{p}} = \sqrt{\frac{2}{3}\mathrm{D_p} : \mathrm{D_p}} \tag{3.26}$$

$$\dot{\varepsilon}_{\mathrm{f}} = [\mathrm{D}_1 + \mathrm{D}_2 \exp(\mathrm{D}_3 \sigma^*)]\,[1 + \mathrm{D}_4(\ln \dot{\varepsilon}^*)]\,[1 + \mathrm{D}_5 \mathrm{T}^*] \tag{3.27}$$

In (3.27) ε_{f} represents the equivalent plastic strain at fracture, ε_{p} is the effective plastic strain, $\dot{\varepsilon}_{\mathrm{p}}$ is the effective plastic strain rate, $\dot{\varepsilon}_{\mathrm{p}}^*$ is the ratio of effective plastic strain rate to reference strain rate as already given in (3.17). $\mathrm{D_p}$ is the plastic rate tensor, and D_1,... D_5 are empiric parameters. When the damage parameter D reaches 1, the element fails. The damage parameter can also be defined to develop in continuously with the stress to describe the weakening of the material [22].

3.3.3 Modified Johnson-Cook Model and Cockroft-Lathan Failure Criterion

In LSDYNA® Modified Johnson-Cook model uses the Cockroft-Latham failure model. This model calculates the flow stress by:

$$\sigma_{\mathrm{eq}} = \left(\mathrm{A} + \mathrm{B}\varepsilon_{\mathrm{eq}}^{\mathrm{n}}\right)\left(1 + \frac{\dot{\varepsilon}_{\mathrm{p}}}{\dot{\varepsilon}_0}\right)\left(1 - \mathrm{T}^{*\mathrm{m}}\right) \tag{3.28}$$

where A, B, C, n and, m are material parameters as mentioned in subsection 3.2.1. $\varepsilon_{\mathrm{eq}}$ is the equivalent plastic strain and $\frac{\dot{\varepsilon}_{\mathrm{p}}}{\dot{\varepsilon}_0}$ is the normalized equivalent plastic strain-rate. The Cockcroft-Latham failure criterion is based on both stresses and strains, so the plastic work becomes an essential factor. It is defined as plastic work per unit volume as:

$$\mathrm{D} = \frac{1}{\mathrm{W}_{\mathrm{cr}}}\int_0^{\varepsilon_{\mathrm{eq}}} (\sigma_1, 0)\mathrm{d}\varepsilon_{\mathrm{p}_{\mathrm{eq}}} \tag{3.29}$$

σ_1 represents the maximum principal stress and W_{cr} is the Cockroft-Latham parameter, which denotes the total plastic work. Employing the Modified Johnson-Cook model, failure of the element starts when D=1. Comparing this model with the Johnson-Cook model, the most important differences are the strain rate dependence term and failure criterion [7]. Johnson-Cook (J-C) model needs five input parameters, which are $\mathrm{D}_1, \mathrm{D}_2, \mathrm{D}_3, \mathrm{D}_4, \mathrm{and}\mathrm{D}_5$ for damage modeling, whereas the Cockroft-Latham (C-L) failure model needs only one parameter. The C-L failure model can be generated by doing a simple uniaxial tensile test. The area under the stress-strain graph gives the limiting W_{cr} (plastic work equals to strain energy), and other The Johnson-Cook parameters can be found by the same procedure explained in subsection 3.2.1. Compared to the procedure for the determination of J-C failure parameters, C-L failure model needs less effort to obtain material model and failure. To be able to identify material parameters more easily, the C-L failure model is selected in this study.

CHAPTER 4

BALLISTIC IMPACT EXPERIMENTS OF HIGH STRENGTH ALUMINUM

This chapter presents the setup of the ballistic experiments conducted and the corresponding results.

4.1 Configuration and Experimental Setup and Results

Ballistic tests were performed in the ballistic laboratory of FNSS with a 20mm fragment simulating projectile (FSP) for strike velocites in the range 800-960m/s. Technical drawings and dimensions of 20mm projectile are given in Figure 4.1. The reason behind using the 20mm FSP is to simulate the artillery threat, which corresponds to Protection Level 4 and 5 in STANAG4569 [3] standards. Dimensions and weight of 20mm FSP have to assure the values given in the drawing and table provided in Figure 4.1. The 20 mm FSP is mandatory for Protection Levels 4 and 5 component acceptance tests [32].

In Table 4.1, the protection level for bullet velocity and type is shown. Level-3 protection level covers a maximum of 770m/s strike velocity with 20mm FSP. Beyond this velocity, protection levels are Level 4 and Level 5 for 20mm FSP. In order to evaluate the protection Level 4 and Level 5, the projectile velocity is set between 800-960m/s in the experiments.

An overview of ballistic laboratory, gun barrel, and impact velocity measurement screens are shown in Figure 4.2.

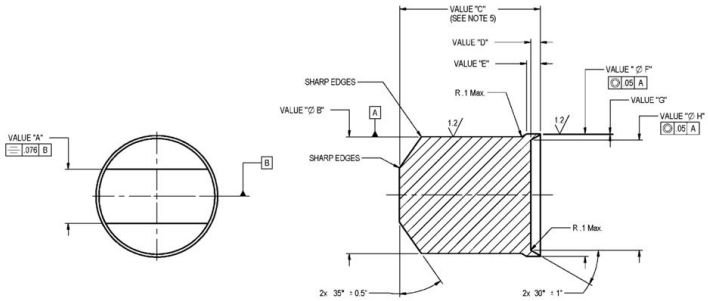

Fragment	Weight(g)	A(mm)	ØB (mm)	C(mm)	D(mm)	E(mm)	ØF (mm)	G(mm)	ØH (mm)
12.7mm	13.4±0.13	5,69-0,4	12,57±0,05	15,24	1,15±0,05	1,47±0,05	12,75+0,08	0,13max	11,43±0,05
20mm	53,8±0,26	9,27-0,4	19,89±0,05	24	1,62±0,05	2,31±0,05	20,83+0,08	0,2max	18,80±0,12

Figure 4.1: The dimension of 12.7mm and 20mm fragment simulating projectile [3].

Table 4.1: Velocity levels for protection levels in STANAG4569 [3]

STANAG 4569 Protection Level	Kinetic Energy Threat	Bullet Type	Artillery Threat (FSP 20mm)
1	Riffle	7.62x51 NATO Ball (Ball M80) Distance 30m Velocity 833 m/s	20 MM FSP Velocity 520 m/s tolerance +/- 20m/s
2	Infantry Rifle	7.62 x 39 API BZ Velocity 695 m/s	20 MM FSP Velocity 630 m/s tolerance +/- 20m/s
3/3+	Sniper Rifle Medium Machine Gun	7.62 x 51 AP (WC core) 7.62 x 54R B32 API (Dragunov)	20 MM FSP Velocity 770 m/s tolerance +/- 20m/s
4	Heavy Machine Gun	14.5x114AP / B32 Velocity 911 m/s	20 MM FSP Velocity Velocity 960 m/s tolerance +/- 20m/s
5	Automatic Cannon	25mm APDS-TM-791 or TLB 073 Velocity 1258 m/s	20 MM FSP Velocity 960 m/s 20 MM FSP Velocity Velocity 960 m/s

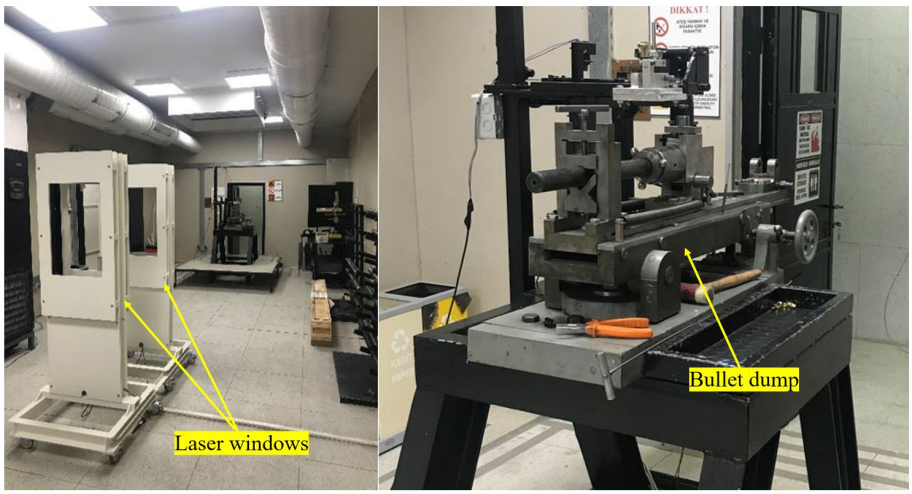

Figure 4.2: An overview of the ballistic laboratory

The projectile passes between two parallel laser windows for the impact velocity measurement. Only the impact velocity of the projectile is measured with the laser system. A high-speed camera is used to measure the exit velocity of a bullet from the target. This fast cam system setup is located in the impact room.

In Figure 4.3 left, demonstration of the impact room is given. In order to cover the high-speed camera from fragment effects of the target plate, an aluminum casing is designed. The aluminum casing is shown in Figure 4.3 (right).

Figure 4.3: Impact room experimental setup (left) and high-speed camera casing (right).

The camera is placed on the side of the target plate such that the camera axis is perpendicular to the trajectory of the projectile. In Figure 4.4 the camera position is shown. This placement is done for the measurement of the residual velocity values with high accuracy. Fragmentation and spall effects are observed with a 30.000 fps high-speed camera with a resolution of 256x176 pixels. Additionally, for target plate positioning, a fixture is designed which is given in Figure 4.5. This fixture holds the target plate from four corners with M16 bolts.

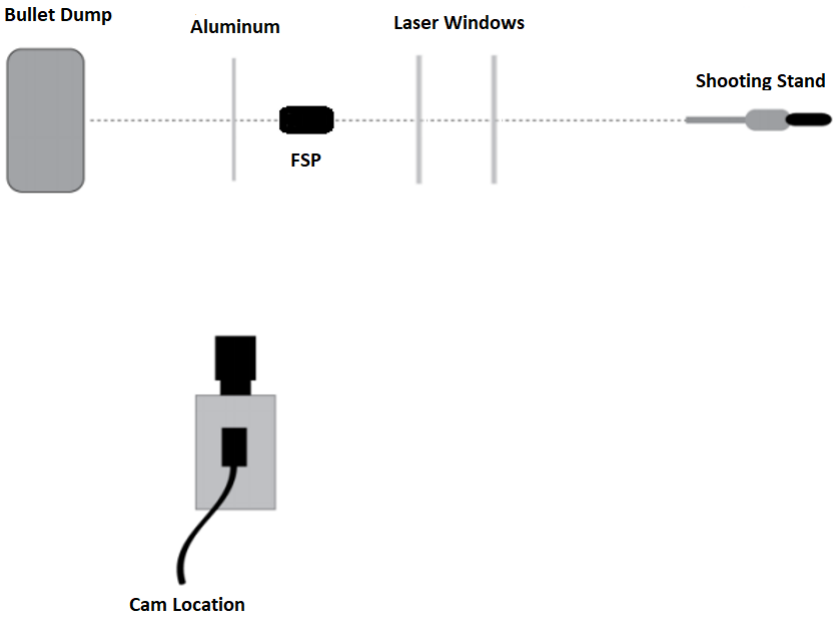

Figure 4.4: Demonstration of camera position to the target plate.

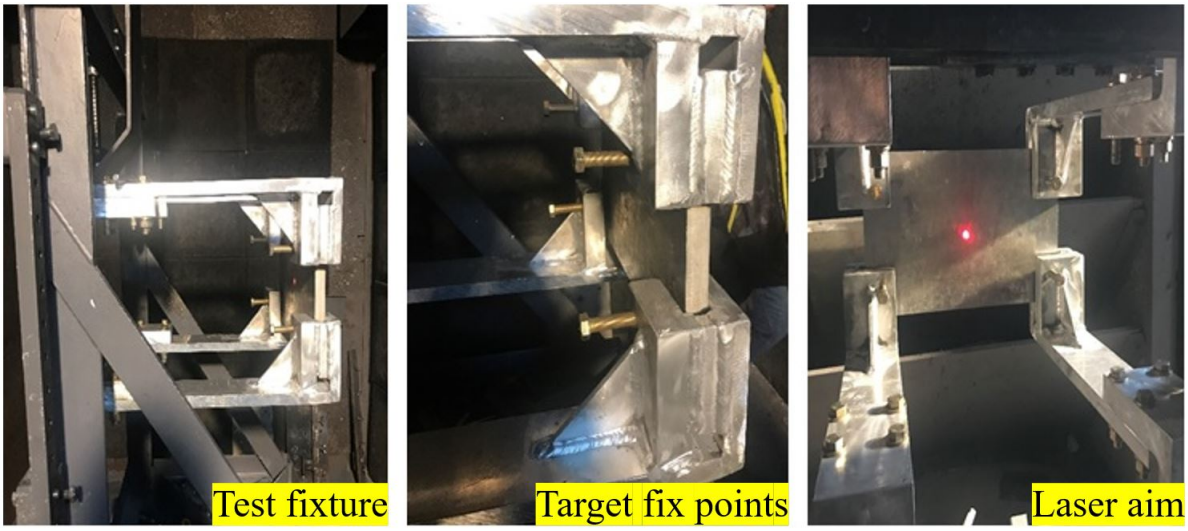

Figure 4.5: Target plate fixture.

Before starting the experiments, a calibration between the high-speed camera measurements and the laser measurement system is needed.

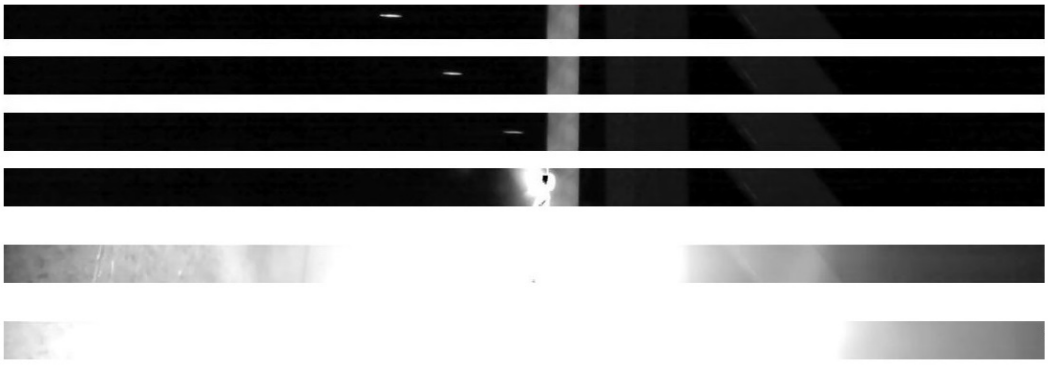

Figure 4.6: High-speed camera images from calibration test.

In Figure 4.6 high-speed camera images are shown from calibration tests. The projectile marching is shown frame by frame for every millisecond until the impact moment. Three shots were performed for calibration studies, and the results are shown in Table 4.2.

Table 4.2: Calibration results

Test Number	Laser Measurements (m/s)	High Speed Camera (m/s)
1	951	903
2	957	909
3	960	912

A strike velocity of 960m/s was used for calibration tests. It is seen that the high-speed camera results are lower than the laser results for about five percent. This information will be later used in the computation of residual velocities.

In measuring the exit velocity of the bullet, difficulties were faced with due to the flare effect. The flare affects the accurate exit velocity measurement because the bullet cannot be captured in the recordings. This situation can be seen in Figure 4.6. To avoid flare effects, a casing was designed, as shown in Figure 4.7. Using this new casing, the tests were performed again. A high-speed camera image of the projectile with a casing setup is also given in Figure 4.7 (below).

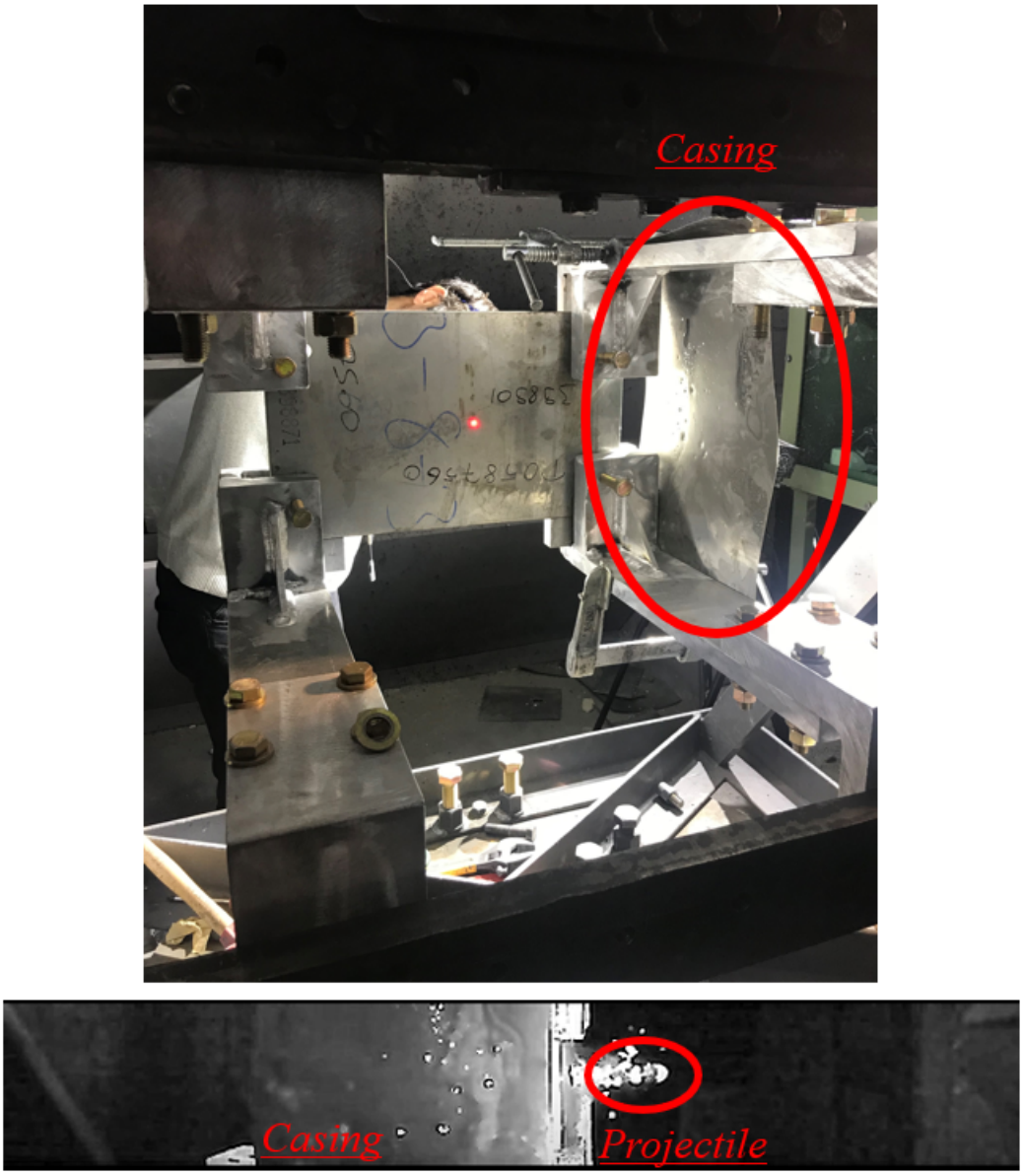

Figure 4.7: The casing to prevent flare effects (above), high-speed camera image of the projectile with casing setup (below).

The target plate is a 300x500mm single monolithic high strength aluminum plate. Three different thickness configurations were tested, which are shown in Figure 4.8. This study only covers monolithic types of targets with variable thickness values, so double-layered or triple-layered armor configurations were not tested.

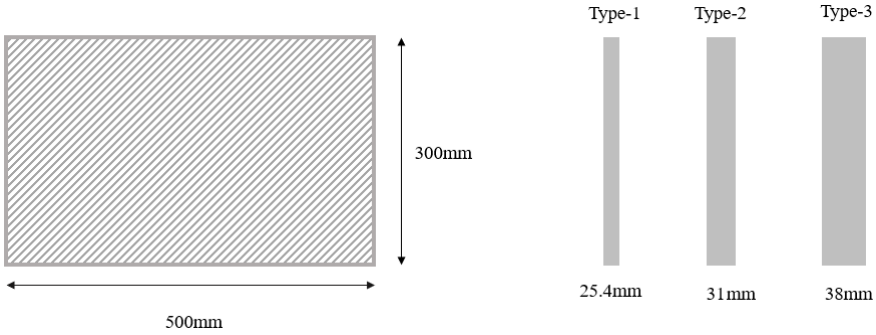

Figure 4.8: Dimensions of target plate and thickness configurations.

The test plan is demonstrated in Table 4.3. These experimental results will be used to validate the numerical model and creating an artificial neural network.

Table 4.3: Ballistic test plan

Number of shots	25.4mm	31mm	38mm
800 m/s	6	2	3
960 m/s	3	4	3

4.2 Experimental Results

Twenty-one shots were performed for ballistic experiments. It was aimed to set the maximum velocity at 960m/s and the minimum velocity at 800m/s. For all shots, residual velocity values were measured. The tests results for different aluminium thicknesses are given in Tables 4.4 to 4.9. In the tables, the results are given for the impact velocities and the residual velocities. The thicknesses of aluminum armors used in tests are 25.4mm, 31mm and 38mm. The zero residual velocity value is shown in Table 4.9 means, the projectile cannot exits from the target plate.

Table 4.4: The results of ballistic experiments for 25.4mm aluminum plate at 960m/s velocity

Test Number	Impact Velocity [m/s]	Residual Velocity [m/s]
1	950	536
2	956	543
3	957	547
Test Average	954	542

Table 4.5: The results of ballistic experiments for 25.4mm aluminum plate at 800m/s velocity

Test Number	Impact Velocity [m/s]	Residual Velocity [m/s]
4	785	385
5	800	410
6	794	394
7	799	411
8	814	418
9	834	429
Test Average	804	407

Table 4.6: The results of ballistic experiments for 31mm aluminum plate at 960m/s velocity

Test Number	Impact Velocity [m/s]	Residual Velocity [m/s]
10	973	417
11	963	406
12	977	431
13	957	404
Test Average	968	414

Table 4.7: The results of ballistic experiments for 31mm aluminum plate at 800m/s velocity

Test Number	Impact Velocity [m/s]	Residual Velocity [m/s]
14	829	310
15	819	306
Test Average	824	308

Table 4.8: The results of ballistic experiments for 38mm aluminum plate at 960m/s velocity

Test Number	Impact Velocity [m/s]	Residual Velocity [m/s]
16	969	237
17	982	247
18	984	270
Test Average	978	251

Table 4.9: The results of ballistic experiments for 38mm aluminum plate at 800m/s velocity

Test Number	Impact Velocity [m/s]	Residual Velocity [m/s]
19	807	0
20	804	0
21	787	0
Test Average	800	0

The plates were perforated in all cases except for the 38mm thickness plate impacted with 800m/s velocity. The perforated aluminum armor plates (25.4mm, 31mm and 38mm) after impact with 960m/s velocity are shown in Figure 4.9.

Figure 4.9: Deformed shape of 25.4mm (left), 31mm (middle), and 38mm (right) plate

The last set of experiments were performed for 38mm thick aluminum armor at 800m/s strike velocity. In the last experiment set, residual velocities were very low or cannot be read because the projectile could not exit from the target. As an example in Figure 4.10 test number 19 is shown.

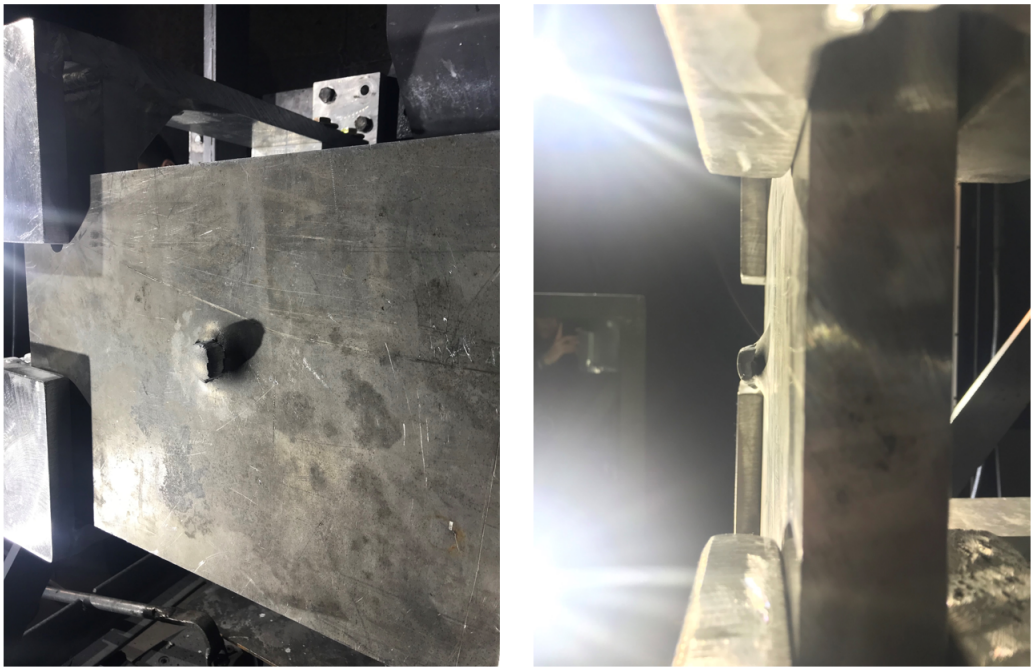

Figure 4.10: 800m/s velocity impact to 38mm aluminum plate

For all experiment sets, average residual velocity values will be compared with the FEA results in Chapter 5.

CHAPTER 5

FINITE ELEMENT ANALYSIS

5.1 Computational Domain and Numerical Setup

Numerical simulations were performed with the explicit solver of LS-DYNA®. Analyses were done for an impact velocity range of 800-960m/s. The model is presented in Figure 5.1.

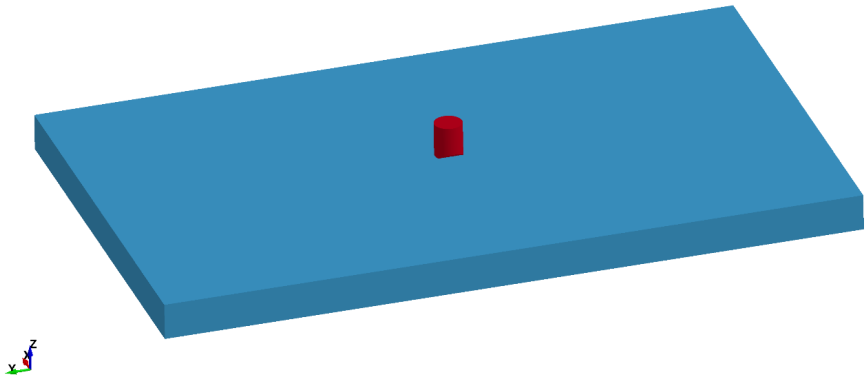

Figure 5.1: The model for impact simulations

The target plate is modeled as 300x500mm high strength aluminum. The thickness of the plate is 25.4mm. The target plate is clamped at the four corners. The MPP LS-DYNA R10.1 solver is selected as a solver version. Owing to the symmetry, only a quarter of the model is simulated. The residual velocity of the projectile is measured with part rigid body velocity option in the preprocessor of LSDYNA®.

The simplified version of the Johnson-Cook material model was used for FSP with 4340 steel material and, the modified Johnson-Cook material model with the Cockroft-

Latham failure model was used for high strength aluminum target material. In order to determine the FSP material model constants of the Johnson-Cook model, it is necessary to perform tests for different speed ranges. Quasi-static tests were performed on a standard strength testing machine for the determination of A, B, n constants. Furthermore, dynamic tests were performed to determine the value of strain rate sensitivity. In this work, the Split Hopkinson Bar test was performed for the strain rate parameters characterization of the FSP material. Thermal effects are neglected for the simplified version of the Johnson-Cook material model. The failure model was not used for the FSP.

Additionally, simple uniaxial tests were performed for the high strength alumınum armor material parameter characterization. The test procedure was used for the target material is the same procedure which is explained in subsection 3.3.3.

The viscous form of hourglass damping (IHQ=6) is used in all analyses, and the effect of the type of hourglass formulation is examined. Also, the viscous form and the stiffness form of hourglass formulation results are compared with residual velocity values. Additionally, hourglass energy values are examined and compared with the internal energy values to select accurate hourglass formulation for further analysis.

5.1.1 Mesh sensitivity

A mesh sensitivity study is performed for four different mesh sizes. The element size is changed through the thickness direction of the target, and residual velocity comparison is made for four different models. The mesh of the FSP is kept the same.

Table 5.1: Residual Velocity Values for different mesh sizes

Model Number	Number of elements Through Thickness Direction	Residual Velocity [m/s]
1	15	510
2	30	570
3	42	576
4	60	577

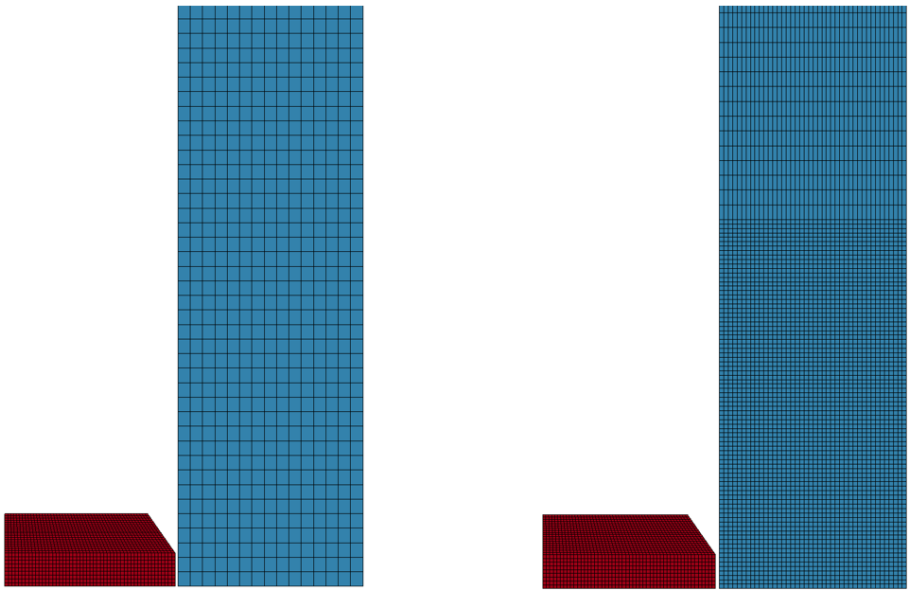

Figure 5.2: The coarsest mesh (left) and the finest mesh (right) used in mesh sensitivity analyses.

In Figure 5.2, the finest mesh, and the coarsest meshes are shown. Note that in Figure 5.2 not the entire target plate, but only the region close to impact is visualized. The FE mesh of the impact region of the target plate consists of 0.2x0.3mm reduced integration hexahedron elements for the finest mesh model, whereas in the coarsest model, the mesh size is 1.6x1.6mm. Elements away from the impact region have larger sizes.

In Table 5.1 and Figure 5.3, residual velocity values for different mesh sizes are shown. Model number one behaves stiffer compared to other three mesh models. Except model number one, all three models give very similar results.

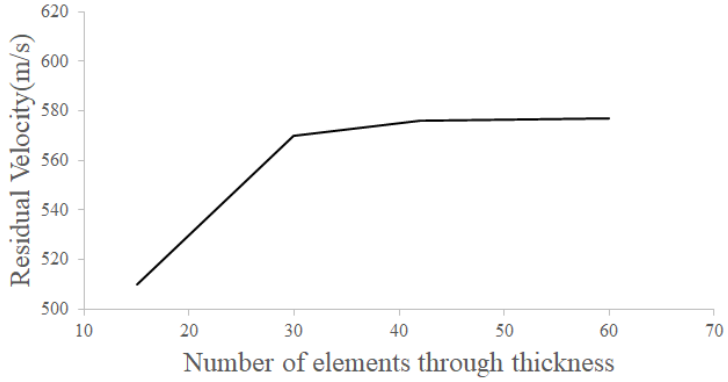

Figure 5.3: Mesh sensitivity results

Although the model two and three give similar residual velocity values, model three gives better crater shapes when compared to model two. Results of the model three and model four are very similar in terms of the residual velocity and the crater shapes. The size of the elements in the thickness direction is vital in the event of tracing the material's behavior through the penetration process.

Additionally, all models are examined by their crater shape results. The crater shape is another critical parameter in ballistic impact simulations. A comparison is made with the quarter model, and results of the coarsest and the finest models are shown in Figure 5.4. Larger elements may create an artificial eroding effect in the simulation and, therefore, lead to larger crater size. According to residual velocity values and crater shape results, model three is founded as the most suitable numerical model for further simulations.

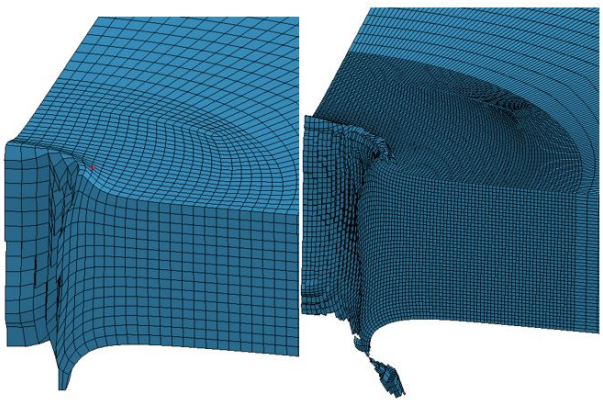

Figure 5.4: Crater shapes of the coarsest mesh and the finest mesh

5.2 Hourglass Solutions

The hourglass and element type selection could affect the accuracy of simulations. In this section, stiffness based hourglass formulations are compared in terms of their hourglass energy values. A shortcoming of the standard hourglass control (IHQ=1) Type 1 is that the hourglass resisting forces are not orthogonal to the linear velocity field when elements are not in the shape of parallelpipeds. As a consequence, such elements can generate a hourglass energy with a constant strain field or a rigid body rotation. Flanagan and Belytschko [33] developed an hourglass control that is orthogonal to all modes except for the zero energy hourglass modes [7]. Type 4 (IHQ=4) and Type 5 (IHQ=5) hourglass algorithms originate from the Flanagan and Belytschko hourglass control. Type 5 hourglass algorithm is similar to Type 4, except that the shape function derivatives are evaluated at the centroid of the element rather than at the origin of the referential coordinate system. This method produces the exact element volume [7]. Type 6 hourglass control improves Type 5 by scaling the stiffness such that the hourglass forces match those generated by a fully integrated element control [7].

This study aims to find the maximum hourglass energy among all types of hourglass formulations. The lowest energy value means the best formulation, which prevents non-physical hourglass problems.

The standard hourglass damping formulation with a coefficient of 0.1 is compared with three forms of stiffness based hourglass algorithms that exist in LSDYNA®. A comparison is made for the residual velocity values and the hourglass damping energy values. In Table 5.2 residual velocity comparison is made among all hourglass formulations.

Table 5.2: Residual velocity values for different hourglass formulations

Hourglass Control	Residual Velocity [m/s]
IHQ=1	576
IHQ=4	577
IHQ=5	578
IHQ=6	581

Deformed shapes of each hourglass formulation are shown in Figure 5.5. The damping coefficient is set to a constant value of 0.1 for each formulation.

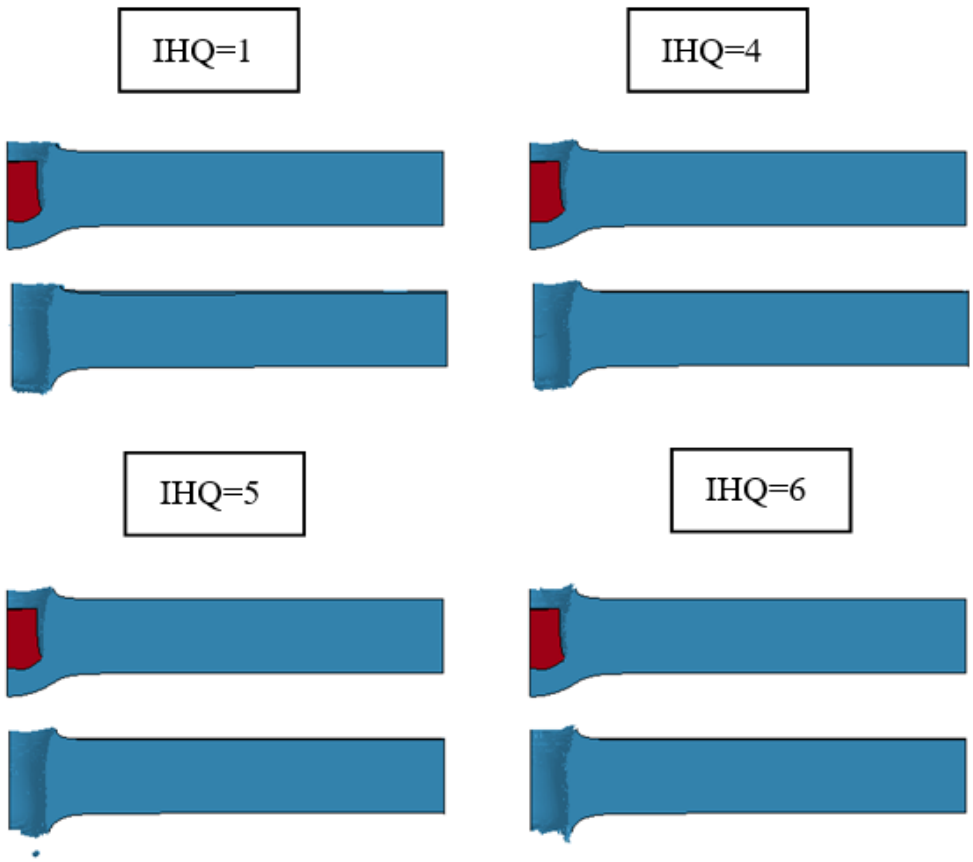

Figure 5.5: Perforating state and final state of the model for each hourglass formulation

Also, the amount of hourglass damping energy is compared for each formulation. In

Figure 5.6 comparison of the hourglass, energy is shown. It is seen that IHQ=1 adds significantly more energy to the system compared to the other damping formulations. Hourglass energies for IHQ=4 and IHQ=5 are very similar. Type six (IHQ=6) shows the best results among all hourglass formulations.

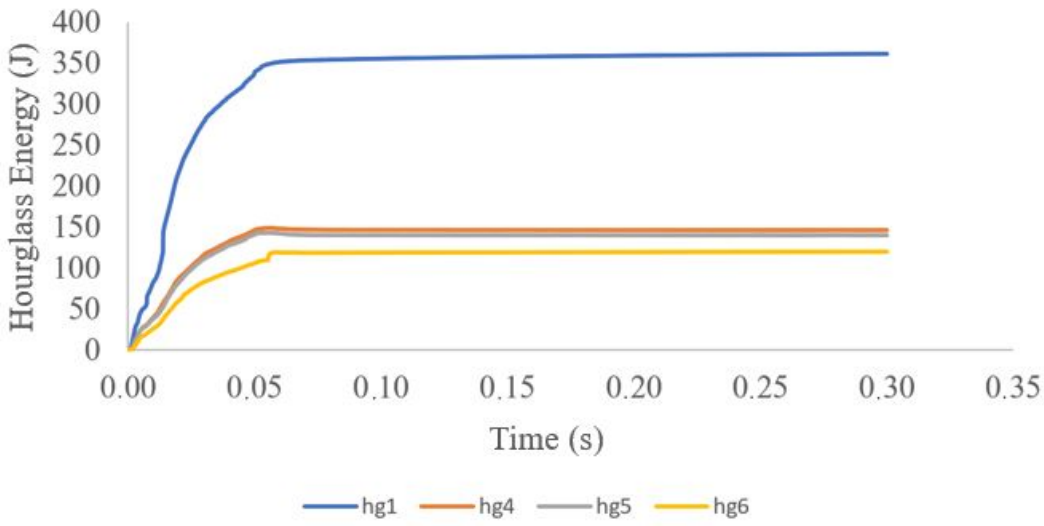

Figure 5.6: Hourglass energy comparison

5.3 Element Type Solutions

In this section, the comparison of residual velocity values is presented for fully integrated elements and one-point integration elements. This element formulation study aims to find the robust element formulation for this impact simulations. LSDYNA® contains four different element formulations (ELFORM=1, -1, -2, and 2), which are used for explicit dynamic impact analysis. ELFORM 1 represents the one-point (reduced) integration element, and ELFORM -1, ELFORM -2, and ELFORM 2 represent the full integration elements. The full integration formulations ELFORM -1 and ELFORM -2 may offer an improved behavior over the formulation in the ELFORM 2 by accounting for poor element aspect ratios in a manner to reduce the transverse shear locking effects in formulation ELFORM 2. ELFORM-1 is a more computationally efficient implementation of ELFORM -2. However, ELFORM-1's resistance to a particular deformation mode, similar to an hourglass mode, is weakened [25].

In Figure 5.7, a comparison of reduced integration and fully integration solid element is shown. Black points at the corner of an element represent the nodes, and red crosses represent the integration points. ELFORM 1 has one integration point whereas others have eight integration points. This difference directly affects the computational cost because fully integrated elements need significantly more computation time. Detailed information about fully integration element types is given in [7]. Very close crater shapes are observed in analysis results among all element types.

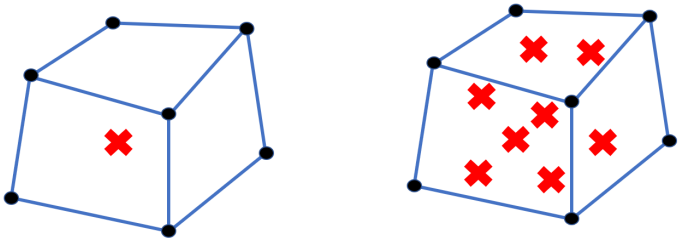

Figure 5.7: Reduced integration and fully integration elements

In Figure 5.8, deformed plates after the impact are shown.

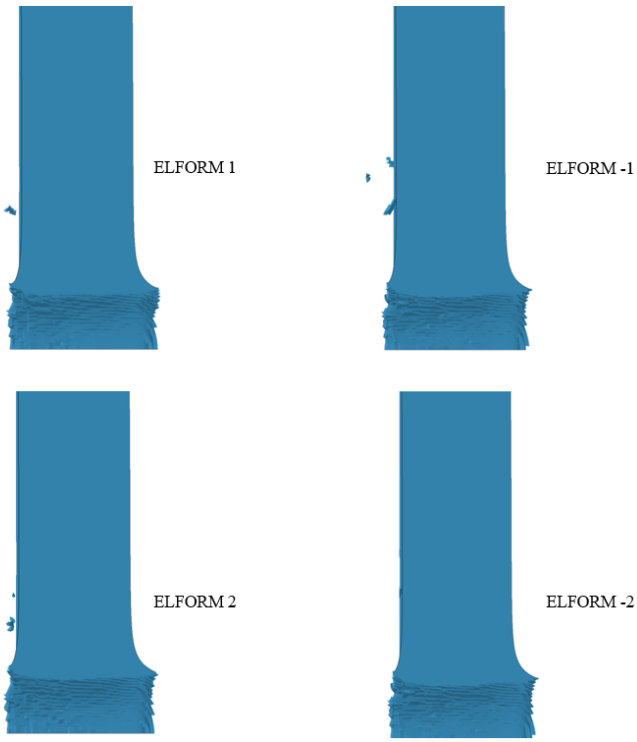

Figure 5.8: Deformed shapes of each element formulation

Additionally, elements formulation effects were analyzed for residual velocity val-

ues of the projectile. In Table 5.3 residual velocity results of each element formulation are shown. Close results are seen between all element formulation. The maximum difference in residual velocity is in the order of 1.8 percent. As a result, similarities are seen in both residual velocity and crater shape results. Therefore ELFORM 1 is selected for further applications to reduce computational time.

Table 5.3: Residual velocity values for each element formulations

ELFORM	Residual Velocity[m/s]
1	576
-1	574
2	574
-2	577

5.4 Analysis results and experiment comparison

In this section, for each set of experiments, average of the residual velocity values is compared with the FEA results. The impact velocity of the FE model is set to the average impact velocity in the related experiment. Detailed perforation results is shown in Appendix A.

5.4.1 Results of 25.4mm aluminum plate

In Figure 5.9, perforation of the FSP to 25.4mm thickness armor, is shown for 954m/s and 804m/s strike velocity cases

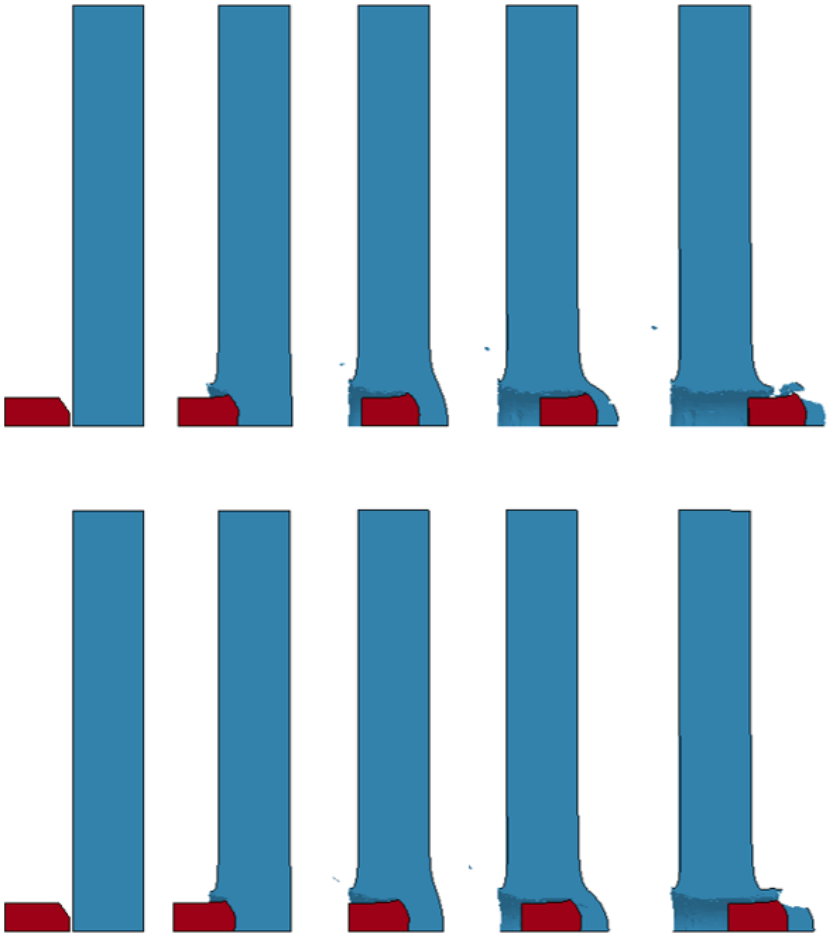

Figure 5.9: Perforation of FSP-25.4mm at 954m/s (above) and 804m/s (below) velocity

In Table 5.4 the residual velocity is presented for 25.4mm thickness armor. In Table 5.4, the residual test velocity represents the average values of all the experiments.

Table 5.4: Residual velocity comparison between FEA and experiment for 25.4mm plate

Analysis Number	FEA Impact Velocity [m/s]	Average Test Impact Velocity [m/s]	FEA Residual Velocity[m/s]	Average Test Residual Velocity[m/s]
1	954	954	560	536
2	804	804	438	407

A good match between experiment and FEA results is obtained for both 954m/s and 804m/s impact cases. There is a 4% percentage difference for the 954m/s strike veloc-

ity case. The difference between exit velocity of test and FEA result is 7% percentage for the 800m/s strike velocity.

Additionally, crater shapes of both experiments and FEA results are compared. In Figure 5.10, crater shapes of the FE analysis, and the experiment are shown for the 25.4mm plate impacted with 804m/s velocity. Note that in Figure 5.10 FE model is solved as a quarter symmetric model, but the results are displayed in full form. Furthermore, crater diameters are measured and compared. From the FEA results, the crater diameter is measured as 33.6mm whereas the experiment is measured as 32.4mm. Similar results obtained for the crater shape and the crater diameter.

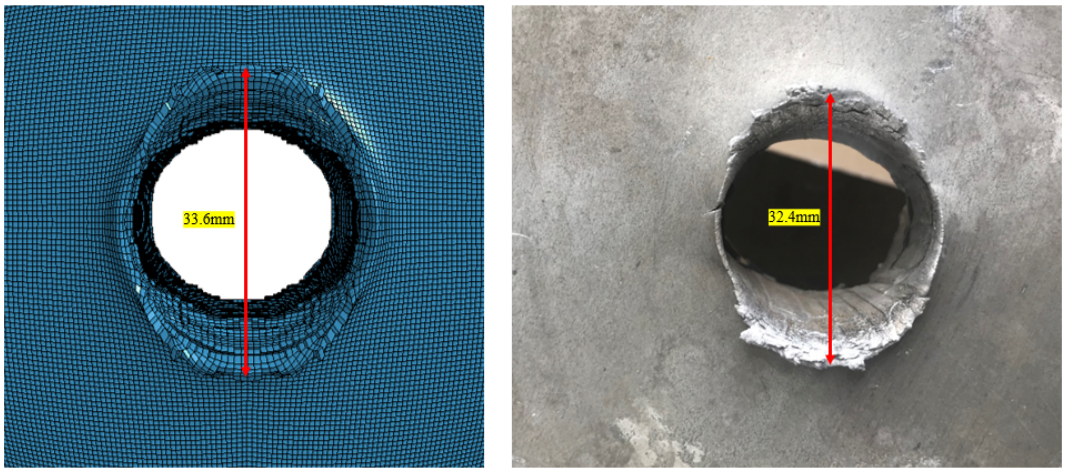

Figure 5.10: Crater shape comparison of 25.4mm plate impacted with 954m/s velocity.

5.4.2 Results of 31mm aluminum plate

In Figure 5.11, perforation of FSP to 31mm thickness aluminum plate is shown for 968m/s, and 824m/s strike velocities.

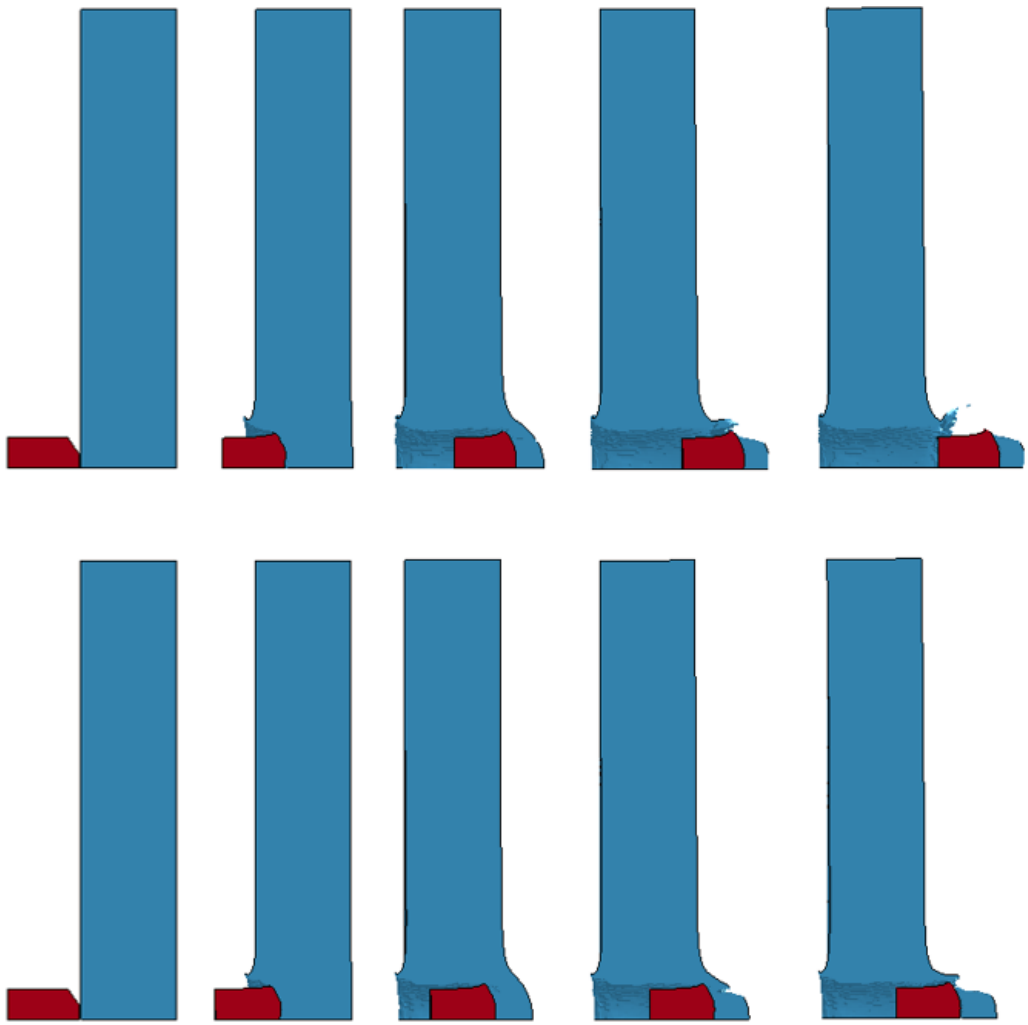

Figure 5.11: Perforation of FSP-31mm at 968m/s (above) and 824m/s (below) velocity cases

In Table 5.5, the residual velocities is presented. A good agreement is found in terms of residual velocity values between the test and the FEA results. In the case of 968m/s impact case, 9% percentage difference is seen between the test and the FEA. Similarly, in the 824m/s impact case, 8% variation is observed between the experiment and the FEA results.

Table 5.5: Residual velocity comparison between FEA and experiment for 31mm plate

Analysis Number	FEA Impact Velocity [m/s]	Average Test Impact Velocity [m/s]	FEA Residual Velocity[m/s]	Average Test Residual Velocity[m/s]
3	968	968	452	414
4	824	824	335	308

Furthermore, the crater shape comparison is made for the 31mm plate impact scenario. In Figure 5.12, the crater shape for a 31mm plate at 960m/s velocity is shown for both the experiments and the FEA. The measured crater diameter is 34.2mm for the FEA and 33.8mm for the experiment. VIn conclusion, close results are found both for the crater shape and the diameter values between the FEA and the test results.

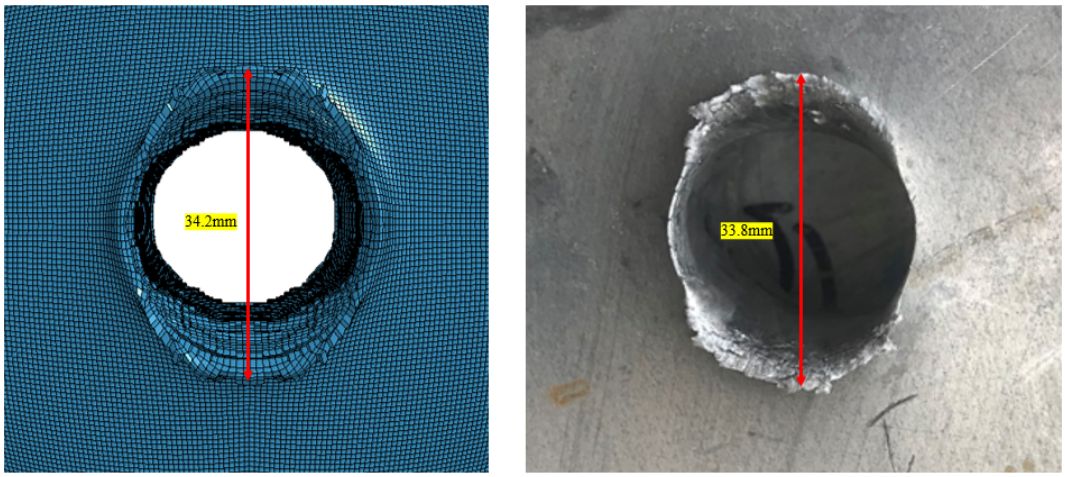

Figure 5.12: Crater shape comparison of 31mm plate

5.4.3 Results of 38mm aluminum plate

In Figure 5.13 perforation of FSP to 38mm thickness aluminum plate is shown for, 978m/s, and 800m/s strike velocities.

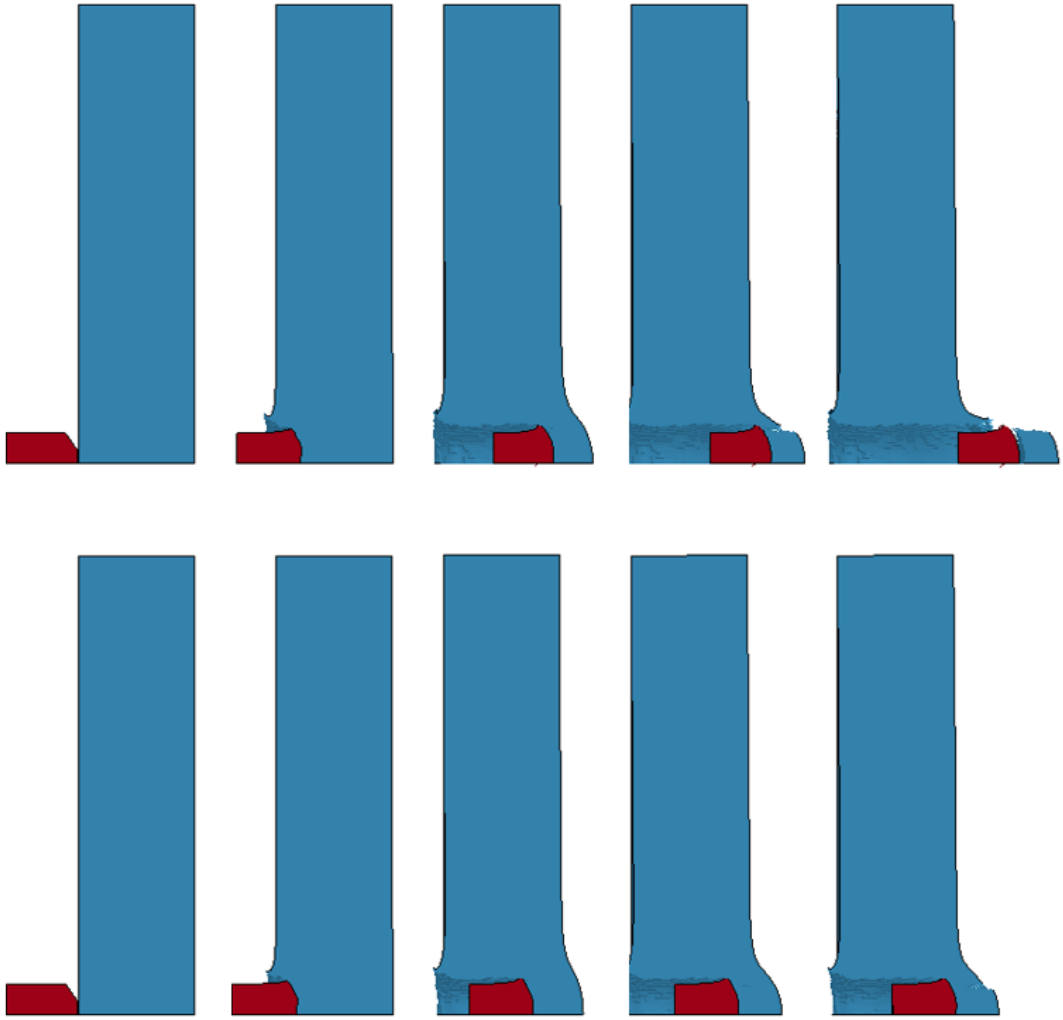

Figure 5.13: Perforation of FSP-38mm at 978m/s (above) and 800m/s (below) velocity case

In Table 5.6 residual velocities is presented. For the first impact case (978m/s), the difference between the test and FEA is found as 6% for the residual velocities. In the second impact scenario (800m/s), FSP cannot exit from the target plate in both the experiments and the FEA.

Table 5.6: Residual velocity comparison between FEA and experiment for 38mm plate

Analysis Number	FEA Impact Velocity [m/s]	Average Test Impact Velocity [m/s]	FEA Residual Velocity[m/s]	Average Test Residual Velocity[m/s]
5	978	978	266	251
6	800	800	0	0

The depth of penetration values is measured for the 800m/s case. For the experiment, the depth of penetration value is found as 38mm, whereas, in FEA gives 38.3mm. In Figure 5.14 and 5.15 different views of the deformed aluminum plate are shown for the test and the FEA.

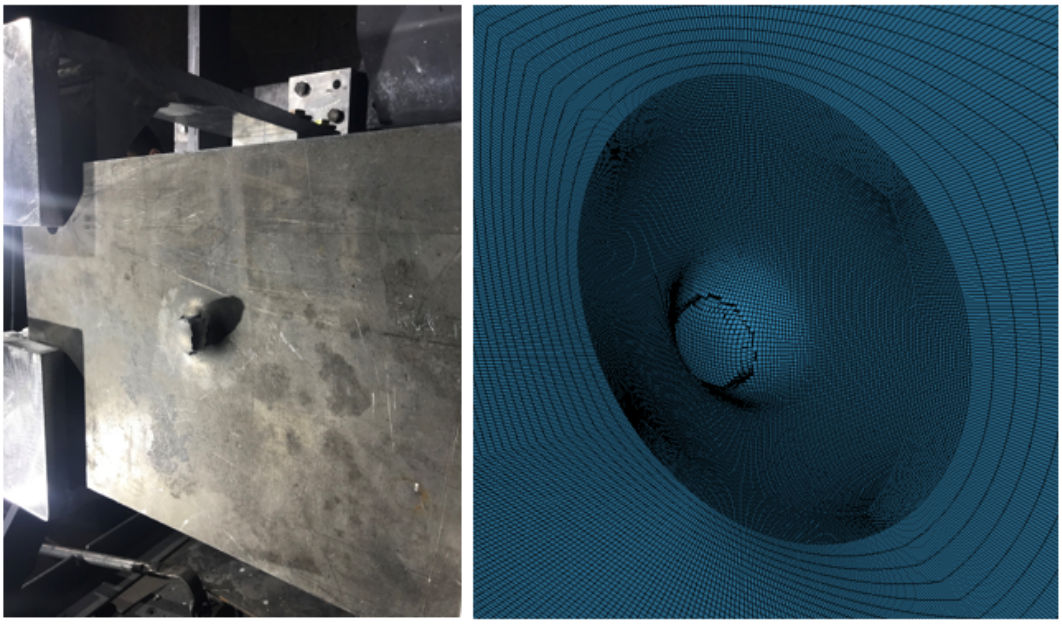

Figure 5.14: 38mm plate 800m/s test (left) and analysis (right) results

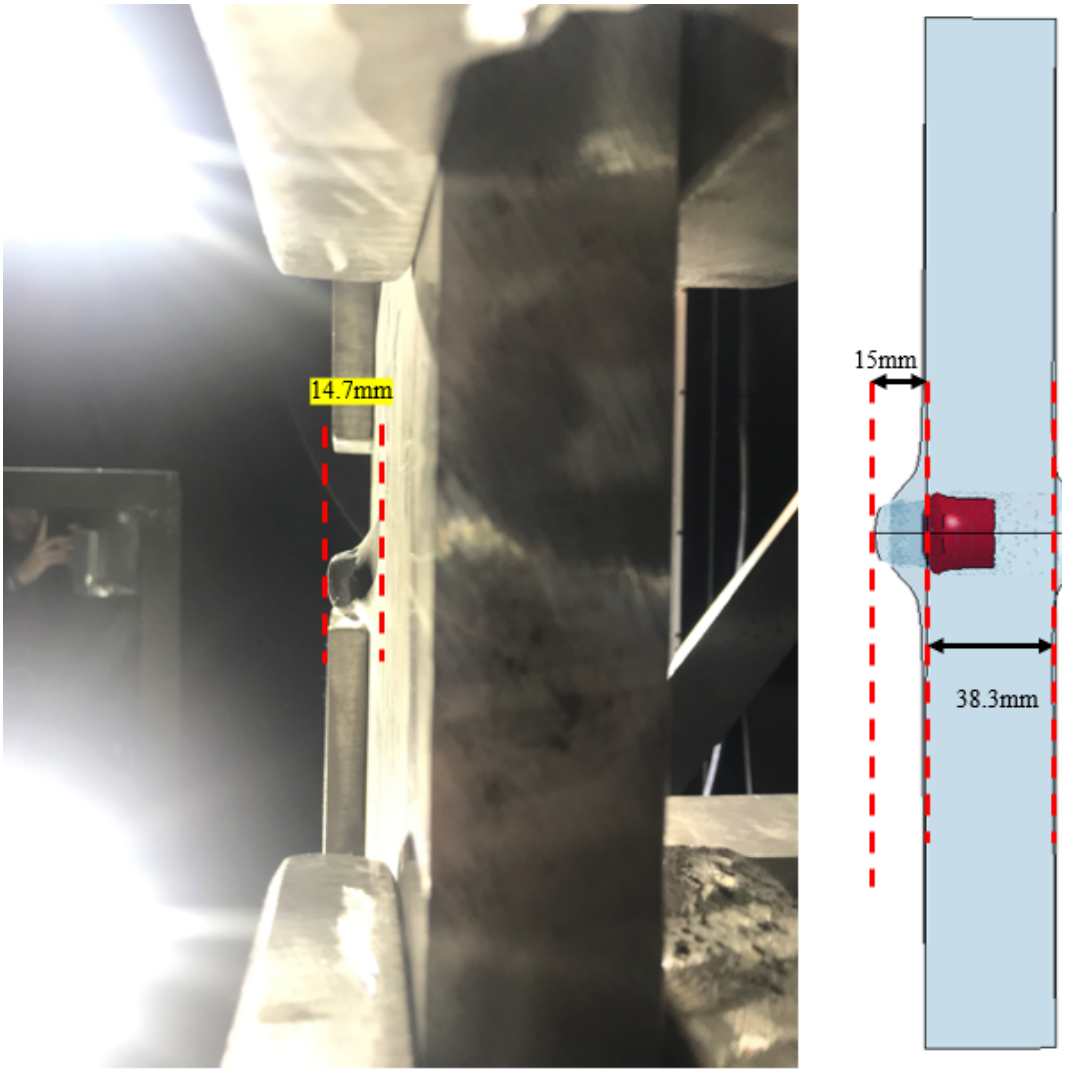

Figure 5.15: 38mm plate 800m/s test (left) and analysis (right) results comparison

Additionally, backplane deflection values are measured, and 0.3mm variation was seen between test and numeric model results. The backplane deflection measurement is shown in Figure 5.15. In the test case, backplane deflection is measured as 14.7mm, whereas numeric model gives 15mm.

Looking at both residual velocity and depth of penetration results, good correlation is seen between FEA and experiment. The FEA model is validated with this comparison study for the 38mm plate case.

CHAPTER 6

ARTIFICIAL NEURAL NETWORK

Artificial neural networks (ANN) connected to a set of data-processing techniques which are used to find solution patterns or models from a sufficient amount of information. Additionally, other benefits can be shown by creating a hybrid solution with the FE method, which can give data to create ANN. Machine learning algorithms can be used to solve complex problems in a very short time. Although the ANN is widely used for many engineering problems, there are very few studies which contain ballistic impact problems. Fernandez-Fdz and Zarea [34] developed a tool to predict ceramic-metal armor ballistic performance by using a combined FE-ANN method. They performed 200 impact scenario FE analyses to create ANN and 7.5% percentage difference was found for residual velocity values between analyses and ANN results.

Similarly, Garci-Crespo [35] studied the performance of steel armors and created different analysis cases for projectile radius, length of the projectile and thickness of the target. The residual mass and the residual velocity values were taken as outputs for each analysis and all these results were used to train an ANN. As a result, a good correlation was seen between analyses and ANN results. Gonzales-Carrasco et al. [36] worked on various neural network types, and compared training algorithms, error cost functions and data selection methods for ballistic problems. Their study showed that ANN is a suitable tool for ballistic limit problems. In this study, 18 ballistic experiments and 60 FE analyses were performed to build an ANN. First, experimental results were used to validate the numerical model results than all 60 ballistic analysis results were used as input for the ANN.

6.1 Theory of Artificial Neural Network

Neural networks are constituted from simple components which work in parallel. These components have so many similarities with a human learning system. They contain three parts of layers, which are represented in Figure 6.1.

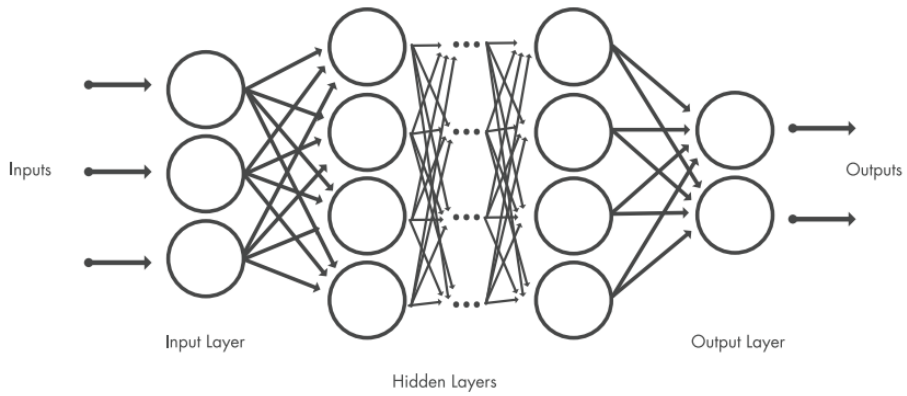

Figure 6.1: The multilayer structure of ANN [10]

Input layers, hidden layers, and output layers are linked through named nodes, or neurons and each hidden layer uses the output of the previous layer as input.

The function of the input layer is to keep all the parameters and data as input and transfer these data to the hidden layer. Then, the hidden layer takes the data from the input layer and processes it to transfer all the data to the output layer. Lastly, the output layer shows the results of hidden layer calculations. The computational power of ANN is determined by the number of neurons or hidden layers used in the setup. The optimum number of neurons or hidden layers can only be found by a trial and error method [37].

In Figure 6.2, the calculation steps of a straightforward neuron are shown. Inputs are represented by x_1, x_2 and x_3 and weights are represented by w_1, w_2 and w_3. Each input has its weight parameter during operations, and weight parameters are the only parameters that change during the learning process. Weight parameters provide a connection between two neurons during the process. At the beginning of the calculation, each input parameter is multiplied by the weight parameter and summed with a bias

value, then this value, and then is sent to the activation function in order to prepare the neuron to output. The activation function usually used to convert the total calculated value to a number between 0 and 1. The sigmoid function is generally used for the activation function phase [10].

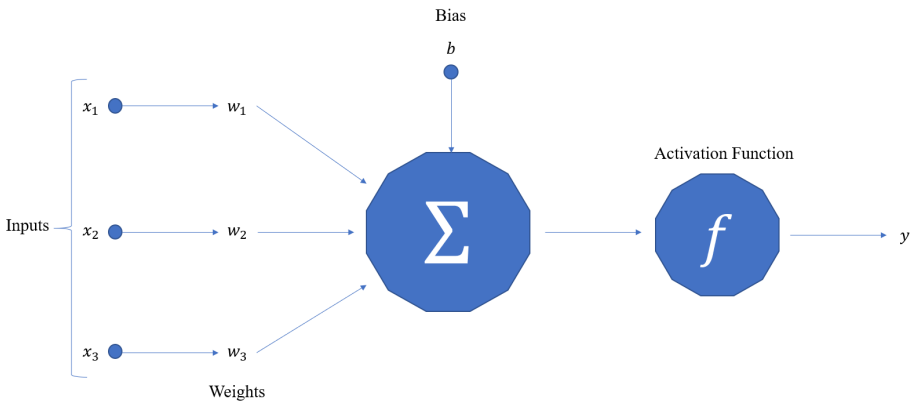

Figure 6.2: One neuron calculation of ANN

Another significant point is in the ANN application is the backpropagation algorithm. The weight parameter variation is processed with backpropagation. The backpropagation method controls how the output changes according to weight change and calculates an error value for each weight value. To minimize the error value, fine-tuning operations are performed on the weight value. A detailed explanation can be found in [10].

In this study, the Levenberg- Marquardt backpropagation algorithm is used. Training of ANN stops when the mean square error of data samples increases. The mean squared error (MSE) is calculated by the difference between output and target values. Therefore, the MSE values close to zero indicate less error for output.

In (6.1), MSE calculation of the ANN for this work is shown. N represents the number of samples, k represents the number of the input set,$\mathrm{V_{FEA}}$ represents the residual velocity obtained from FEA analysis (i.e., the actual value), $\mathrm{V_{ANN}}$ represents the residual velocity predicted the ANN model. The square root of (6.1) is defined as the Root Mean Square Error (RMSE) which represents the difference between FEA residual velocity results and ANN residual velocity results. The definition of RMSE is given in (6.2).

$$MSE = \frac{1}{N}\sum_{k=1}^{N}\left(V_{FEA}^{k} - V_{ANN}^{k}\right)^{2} \tag{6.1}$$

$$RMSE = \sqrt{\frac{1}{N}\sum_{k=1}^{N}\left(V_{FEA}^{k} - V_{ANN}^{k}\right)^{2}} \tag{6.2}$$

Additionally, a correlation between output and target is measured by performing the regression analysis. If R-value is close to 1, it means that there is a good correlation between the target and the outputs, whereas zero R-value indicates that a random correlation.

The most crucial feature of the Levenberg-Marquardt algorithm is that it converges much faster than other algorithms. The speed of convergence is much higher than other backpropagation algorithms. Additionally, the Levenberg-Marquardt algorithm provides lower MSE values, so the accuracy of this algorithm is higher than other algorithms [10]. The Levenberg-Marquardt algorithm is selected in this study because of the benefits above.

6.2 ANN Training

The preparation of the ANN is initialized with the 18 FE analyses at various impact velocities. In this study, two input parameters are used in FE analyses, which are the target thickness and the impact velocity. Residual velocity values are measured for all FE analyses. Therefore, the residual velocity values are chosen as output for the ANN training. The set of the performed analyses and results are shown in Table 6.1.

Table 6.1: FE analysis results for various strike velocities

Analysis Number	Plate Thickness [mm]	Impact Velocity [m/s]	Residual Velocity[m/s]
1	25.4	800	436
2	25.4	850	484
3	25.4	875	503
4	25.4	900	525
5	25.4	925	546
6	25.4	960	576
7	31	800	308
8	31	850	358
9	31	875	383
10	31	900	406
11	31	925	429
12	31	960	460
13	38	800	0
14	38	850	92
15	38	875	160
16	38	900	193
17	38	925	229
18	38	960	266

All the inputs and outputs presented in Table 6.1 are embedded in the ANN, and then the training process of ANN is started. Data shown in 6.1 were selected at intervals of 25m/s and 50m/s from 800m/s to 960m/s range. The neural network tool of MATLAB is used for the ANN training. Then, SIMULINK is used for the postprocessing phase. Default parameters for hidden layers and hidden neurons are used for the ANN training. MSE values and regression analysis results are to be examined to check the accuracy of the ANN. The ANN setup is shown in Figure 6.3

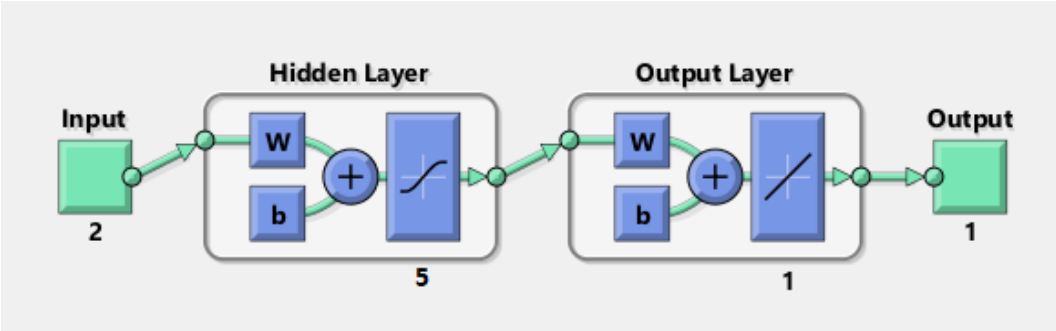

Figure 6.3: Representation of the ANN setup

All the data samples are divided into three groups in MATLAB for the ANN setup. The first set of data is called the training, which is used for the weight and the bias calculation. The other two sets are the validation and the test. The validation and the test data sets are used for the performance checking of the ANN. Default values are used for data participation, so 70% of data is sent to the training, 15% is sent to validation and 15% is sent to the test part. All the training, validation, and test dataset samples shown in Table 6.1 of ANN setup assigned randomly.

In Figure 6.4, the Levenberg- Marquardt algorithm performance graphic is shown. Here epoch number represents the number of sweeps in one forward direction and backward through all training data. According to Figure 6.4, the lowest validation error is taken at the 6th epoch of the training. All of the training, validation, and test MSE values are shown in Table 6.2.

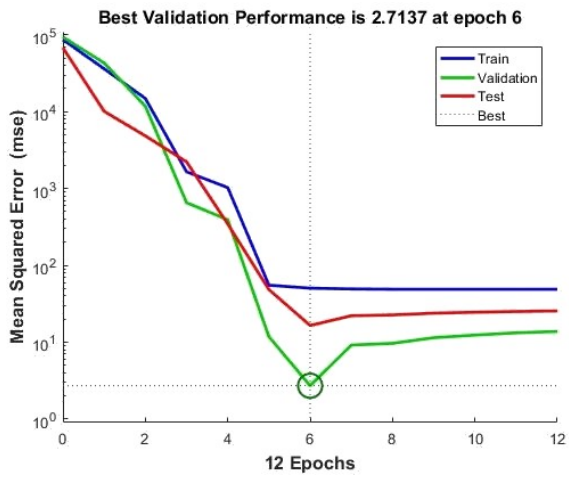

Figure 6.4: Performance of Levenberg- Marquardt algorithm performance.

The lowest validation error is taken at the 6th epoch. The ANN run stops at the 12th epoch to prevent overfitting problems. One of the problems that arises during neural network preparation is called overfitting. Generally, the MSE error decreases as the number of epochs increases; however, MSE can start to increase on the validation data set as the neural network starts to overfit the training data. The early stopping of ANN can prevent overfitting problems [10]. Additionally, the number of neurons which are used in ANN can lead to overfitting results. In Figure 6.5 some of the trial-error studies for ANN performance are shown for 123 epochs and 20 hidden layers of the ANN setup separately.

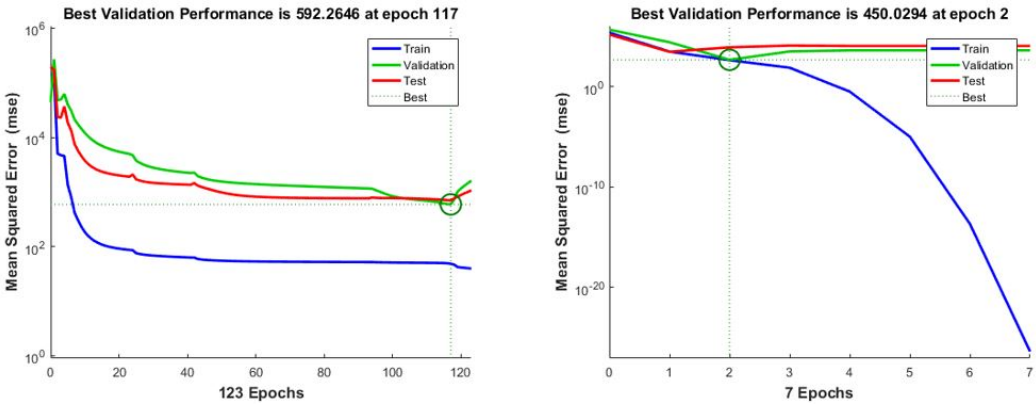

Figure 6.5: 123 epoch results (left) and 20 hidden layers (right) results

In Figure 6.5, the MSE error starts to increase after 117 epoch while the training error decreases. Therefore, it can be seen that the ANN starts to overfit after 117th of the epoch. Also, the MSE values are found for both training and validation data sets. The minimum MSE value is found around 592.26 which is much higher than the MSE value shown in Figure 6.4. Similar overfitting results are seen for the twenty hidden layers ANN setup. The training error starts to decrease after the second epoch while the validation error starts to increase. After the trial-error study for the number of epoch and hidden layers used in ANN, it is concluded that the ANN performance with five hidden layers and twelve epochs can be used for further studies. The MSE values are shown in Table 6.2 for five hidden layers and twelve epoch ANN setup.

Table 6.2: MSE and RMSE Values of Training, Validation and Test data

	Samples	MSE	RMSE
Training	12	50.43	7.1
Validation	3	2.71	1.64
Testing	3	16.5	4.06

The MSE value of the training is 50.43, whereas the validation MSE is 2.71 and the test MSE is 16.5. Additionally, the root mean square (RMSE) values are shown in Table 6.2. As mentioned in Section 6.1, the RMSE values represent the difference between the residual velocity values of the FEA (target) and the ANN (predicted). The average difference between the target and the predicted velocity value is 7.1m/s. Furthermore, the validation and the test MSE and RMSE values are examined. The average difference between the FEA and the ANN results are found as 1.64m/s for the validation and 4.06m/s for the test phase. The maximum difference between the FEA and the ANN residual velocity value is 7.1m/s which is an acceptable difference for ballistic impact problems. According to differences between the target and the residual output, it can be concluded that the ANN gives quite a good correlation between the output and the target.

Additionally, a regression analysis is performed to check ANN performance. In Figure 6.6, the target axis represents the FEA results, and the output axis represents the ANN results. According to the graphics, the FEA and the ANN give quite similar results for the training, test, validation and overall results. In all of the graphics, the R-value is so close to 1 which means a very good correlation is provided between the target and the outputs.

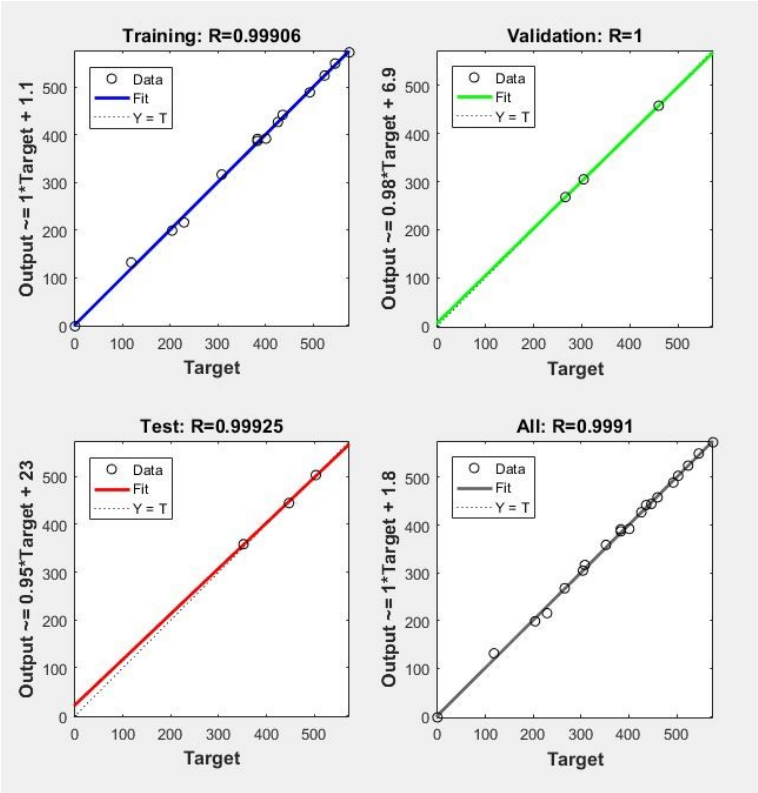

Figure 6.6: Regression analysis results for training, test, validation and overall data.

6.3 FEA and ANN results comparison

Figure 6.7 shows the SIMULINK setup for the ANN. The ANN is performed for different velocities and thicknesses. The velocity range is set between 800m/s and 960m/s, and the target thickness is set according to FE analyses between 25mm and 38mm. The graphical representation of the residual velocity difference between the experiments, FEA and ANN is shown in Appendix A.

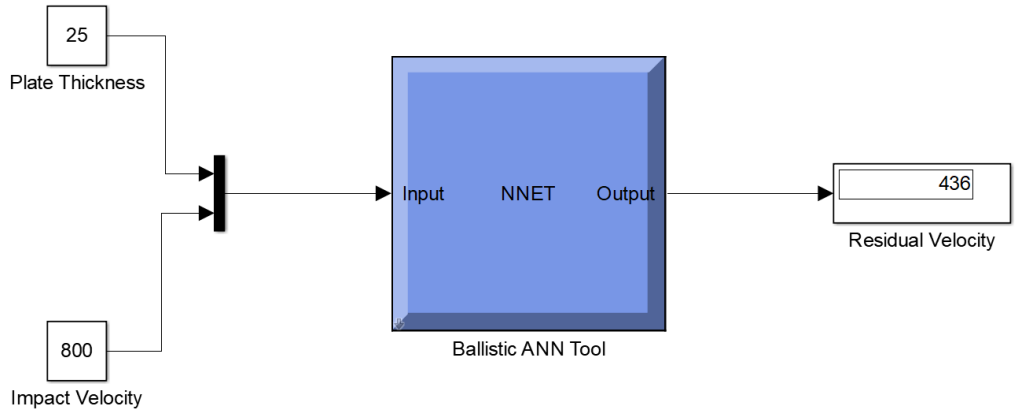

Figure 6.7: ANN Simulink setup for ballistic analysis

After entering the plate thickness and impact velocity parameters the ANN is run, and the residual velocity is obtained. ANN is performed for various thicknesses and impact velocity values. The FE analyses are performed for the cases which are shown in Table 6.3. Also, the ANN is performed for each thickness and impact velocity values shown in Table 6.3. According to Table 6.3, consistent residual velocity results are generated with the ANN. In Table 6.3, difference column represents the difference of ANN results from FEA results. The ANN analyses run about 2-3 seconds for each case, whereas the FEA analyses continue about 8 hours in an eight-core 64GB RAM computer.

Table 6.3: ANN and FEA comparison of residual velocity values

	27mm Thickness Residual Velocity [m/s]			32mm Thickness Residual Velocity [m/s]		
Impact Velocity [m/s]	ANN	FEA	Difference %	ANN	FEA	Difference %
800	415	401	3.49	264	247	6.88
820	433	422	2.61	290	274	5.84
850	457	449	1.78	316	298	6.04
860	466	457	1.97	338	318	6.29
875	478	472	1.27	355	332	6.93
880	481	472	1.91	360	334	7.78
900	496	491	1.02	382	354	7.91
910	503	500	0.60	392	393	-0.25
925	512	512	0.00	407	376	8.24
930	516	516	0.00	411	379	8.44
960	534	541	-1.29	438	411	6.57

In order to show that the results are consistent with the FEA, FE analyses are performed for 27mm thickness and 32mm thickness plates for each velocity, see Table 6.3. These analyses are performed for a comparison between the FEA and the ANN results. According to Table 6.3, a good correlation is found between the ANN and the FEA results. The maximum residual velocity value difference is found around 8.4% for 32mm thickness and 930m/s impact velocity case.

Additionally, the ANN residual velocity results are compared with the experiment results. In Table 6.4, the difference between ANN and experiment is represented. The maximum difference between these two residual velocity result is found around 8.3%. Very close results are also seen between ballistic experiments and ANN results.

Table 6.4: ANN and Ballistic experiment comparison of residual velocity values

Thickness [mm]	Average Test Impact Velocity [m/s]	Average Test Residual Velocity [m/s]	ANN Residual Velocity [m/s]	Difference [%]
25	954	542	569	4.7
	804	407	444	8.3
31	968	414	451	8.2
	824	308	332	7.2
38	978	251	267	5.9
	800	0	0	0

In Figure 6.8 relationship between thickness of the target, impact velocity of projectile and residual velocity values is shown in a response surface graphic.

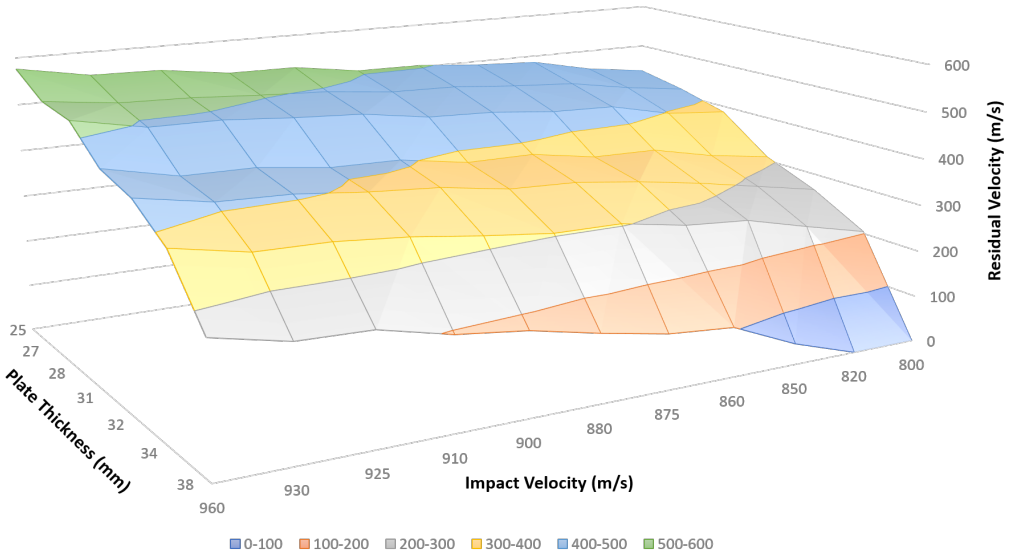

Figure 6.8: Response surface representation of ANN results

CHAPTER 7

SUMMARY AND CONCLUSION

7.1 Conclusion

The study aims to reduce the number of expensive tests and analyses needed, preprocessing and postprocessing times of FE in ballistic studies with the help of a combined FEA-ANN approach. To this end, a tool is proposed by combining FEA and ANN methods to make a quick prediction in aluminum armor design.

First, a numerical model verification study was conducted, and mesh sensitivity, hourglass formulations, and element formulations were examined. The effects of these parameters on the residual velocity values were examined.

At the end of the verification of the numerical model, parameters that have significant effect the on the FE model were determined. After that phase, ballistic experiments were performed to validate the numerical model.

In ballistic experiments, the impact velocity, the residual velocity and the depth of penetration were measured. Additionally, crater shapes and crater diameters were examined in order to make comparisons with the FEA model.

After the ballistic test phase, a comparison of FEA results and ballistic test results was performed. At first stage of comparison, the residual velocity values were controlled. The maximum difference in residual velocity values was found around 9% percent. A good correlation was seen between the residual velocity values for each target thickness and impact velocity.

Furthermore, the crater shape, the crater diameter, the depth of penetration and the

backplane deflection values were compared.

Then, additional analyses were performed to expand the ANN database. All the additional FEA results were added into the ANN database and then ANN runs were performed for different thickness and impact velocity values. ANN analyses showed reasonable results which were found to be consistent with FE analyses. For 27mm plate thickness case, the residual velocity difference was founded as maximum 3.49% whereas for 32mm plate thickness, the residual velocity difference was founded maximum 8.49%. Therefore, the ANN ballistic tool can be used for the preliminary design of an aluminum armor for the determination of the armor thickness.

7.2 Future work

This study was performed for a single layer armor plate made of high strength aluminum material within a defined thickness range. This ANN model will be extended for double-layered and tree-layered armor combinations in the future. This was the main reason for choosing the ANN for this study. In the concept design stage, double-layered or three-layered armor designs were also evaluated for armor plates. Double-layer and three-layer ballistic armors were also created using a steel-aluminum combination. The procedure followed in this study could be applied to double-layered and three-layer aluminum armors to expand the ANN database. Input parameters of the ANN could contain double-layer and three-layer armor designs. Also, the weight of the armor could be added as output of the ANN model to determine the armor performance together with the weight. In Steel-Al combined armors, the weight of total armor is a very significant point for the armor design. Design of experiment approach will be used to optimize back-propagation of the ANN parameters, so, the accuracy of the ANN residual velocity results can be increased. Additionally, new graphical user interface can be organized to make the tool more user-friendly.

REFERENCES

[1] C. L. Rao, V. Narayanamurthy, and K. R. Y. Simha, *Applied Impact Mechanics*. John Wiley & Sons, Ltd, jun 2016.

[2] J. A. Zukas, *High Velocity Impact Dynamics-Wiley-Interscience 1990*.

[3] NATO and PfP, "Procedures Evaluating Protection Level Logistic Light Armoured Vehicles," *Allied Engineering Publication*, vol. 1, no. FEBRUARY, 2005.

[4] T. Børvik, M. J. Forrestal, and T. L. Warren, "Perforation of 5083-H116 Aluminum Armor Plates with Ogive-Nose Rods and 7.62 mm APM2 Bullets," *Experimental Mechanics*, vol. 50, no. 7, pp. 969–978, 2010.

[5] M. E. Backman and W. Goldsmith, "The mechanics of penetration of projectiles into targets," *International Journal of Engineering Science*, vol. 16, no. 1, pp. 1–99, 1978.

[6] A. L. Eulerian, "LSDYNA ALE Arbitrary Lagrangian Eulerian Traning Notes,"

[7] Livermore Software Technology Corporation (LSTC), *Theory Manual 02/20/19*, vol. 19.

[8] A. Mehmood, "Governing equations," in *Mathematical Engineering*, no. 9783319554310, pp. 13–21, Springer Verlag, 2017.

[9] L. V. Zhigilei, "University of Virginia, Department of Materials Science and Engineering, Introduction to the Science and Engineering of Materials Lecture Notes," *Materials Science*, pp. 1–34.

[10] M. Beale and H. Demuth, "Neural network toolbox," *Neural Network Toolbox, User's Guide*, 2004.

[11] H. Hopkins and H. Kolsky, "In: Proceeding of the 4th Hypervelocity Impact Symposium. APGC-TR-60-39," vol. 1, 1960.

[12] W. Goldsmith, *High-Speed Physics. Springer-Verlag, Berlin,*. 1967.

[13] A. E. Olshaker and R. L. Bjork, "Proceedings of 5th Symposium on Hypervelocity Impact," *Proceedings of 5th Symposium on Hypervelocity Impact*, vol. 1, no. 1, pp. 225–239, 1962.

[14] G. Ben-Dor, A. Dubinsky, and T. Elperin, "Ballistic Impact: Recent Advances in Analytical Modeling of Plate Penetration Dynamics–A Review," *Applied Mechanics Reviews*, vol. 58, no. 6, p. 355, 2005.

[15] O. Arndt, T. Barth, B. Freisleben, and M. Grauer, "Approximating a finite element model by neural network prediction for facility optimization in groundwater engineering," *European Journal of Operational Research*, vol. 166, no. 3, pp. 769–781, 2005.

[16] W. L. Chan, M. W. Fu, and J. Lu, "An integrated FEM and ANN methodology for metal-formed product design," *Engineering Applications of Artificial Intelligence*, vol. 21, no. 8, pp. 1170–1181, 2008.

[17] M. Ostad and A. Mazahery, "The ANN application in FEM modeling of mechanical properties of Al – Si alloy," *Applied Mathematical Modelling*, vol. 35, no. 12, pp. 5707–5713, 2011.

[18] N. Haghdadi, A. Zarei-Hanzaki, A. R. Khalesian, and H. R. Abedi, "Artificial neural network modeling to predict the hot deformation behavior of an A356 aluminum alloy," *Materials and Design*, vol. 49, pp. 386–391, 2013.

[19] R. Hambli, "Numerical procedure for multiscale bone adaptation prediction based on neural networks and finite element simulation," *Finite Elements in Analysis and Design*, vol. 47, no. 7, pp. 835–842, 2011.

[20] P. P. Gudur and U. S. Dixit, "A neural network-assisted finite element analysis of cold flat rolling," *Engineering Applications of Artificial Intelligence*, vol. 21, no. 1, pp. 43–52, 2008.

[21] R. Haj-Ali, H. K. Kim, S. W. Koh, A. Saxena, and R. Tummala, "Nonlinear constitutive models from nanoindentation tests using artificial neural networks," *International Journal of Plasticity*, vol. 24, no. 3, pp. 371–396, 2008.

[22] B. Adams, *Simulation of ballistic impacts on armored civil vehicles,Department of Mechanical Engineering, Eindhoven University of Technology, Netherlands*. PhD thesis, 2003.

[23] M. Dokainish and K. Subbaraj, "A survey of direct time-integration methods in computational structural dynamics—I. Explicit methods," *Computers & Structures*, vol. 32, pp. 1371–1386, jan 1989.

[24] T. J. Hughes and R. L. Taylor, "Unconditionally stable algorithms for quasi-static elasto/visco-plastic finite element analysis," *Computers and Structures*, vol. 8, no. 2, pp. 169–173, 1978.

[25] O. Anderson, "The Gruneisen ratio for the last 30 years, 143, 279-294, 2000," *Geophys. J. Int.,*, pp. 279–294, 2000.

[26] A. Shavit and C. Guthinger, *Thermodynamics, from concepts to applications*, vol. 0132882671. Pearson Education limited, 1995.

[27] Z. Rosenberg and E. Dekel, *Terminal ballistics*, vol. 9783642253058. Springer-Verlag Berlin Heidelberg, april 2012.

[28] M. A. Meyers, *Dynamic behavior of materials*, vol. 047158262X. John Wiley and Sons, Inc. New York, january 1994.

[29] F. E. Prieto and C. Renero, "The equation of state of solids," *Journal of Physics and Chemistry of Solids*, vol. 37, pp. 151–160, jan 1976.

[30] ABAQUS, "Version 6.10-1 Analysis User's Manual," 2017.

[31] C. Kiran Sagar, A. Chilukuri, and A. Priyadrashini, "Determination of johnson cook material model constants for 93% WHA and optimization using genetic algorithm," *Materials Today: Proceedings*, vol. 5, no. 9, pp. 18911–18919, 2018.

[32] Dytran, "Theory Manual 2008 r1," *Analysis*, 2008.

[33] D. P. Flanagan and T. Belytschko, "A uniform strain hexahedron and quadrilateral with orthogonal hourglass control," *International Journal for Numerical Methods in Engineering*, vol. 17, no. 5, pp. 679–706, 1981.

[34] D. Fernández-Fdz and R. Zaera, "A new tool based on artificial neural networks for the design of lightweight ceramic-metal armour against high-velocity impact of solids," *International Journal of Solids and Structures*, vol. 45, no. 25-26, pp. 6369–6383, 2008.

[35] A. García-Crespo, B. Ruiz-Mezcua, D. Fernández-Fdz, and R. Zaera, "Prediction of the response under impact of steel armours using a multilayer perceptron," *Neural Computing and Applications*, vol. 16, no. 2, pp. 147–154, 2007.

[36] I. Gonzalez-Carrasco, A. Garcia-Crespo, B. Ruiz-Mezcua, and J. L. Lopez-Cuadrado, "Dealing with limited data in ballistic impact scenarios: An empirical comparison of different neural network approaches," *Applied Intelligence*, vol. 35, no. 1, pp. 89–109, 2011.

[37] H. M. Gomes and A. M. Awruch, "Comparison of response surface and neural network with other methods for structural reliability analysis," *Structural Safety*, vol. 26, pp. 49–67, jan 2004.

APPENDICES

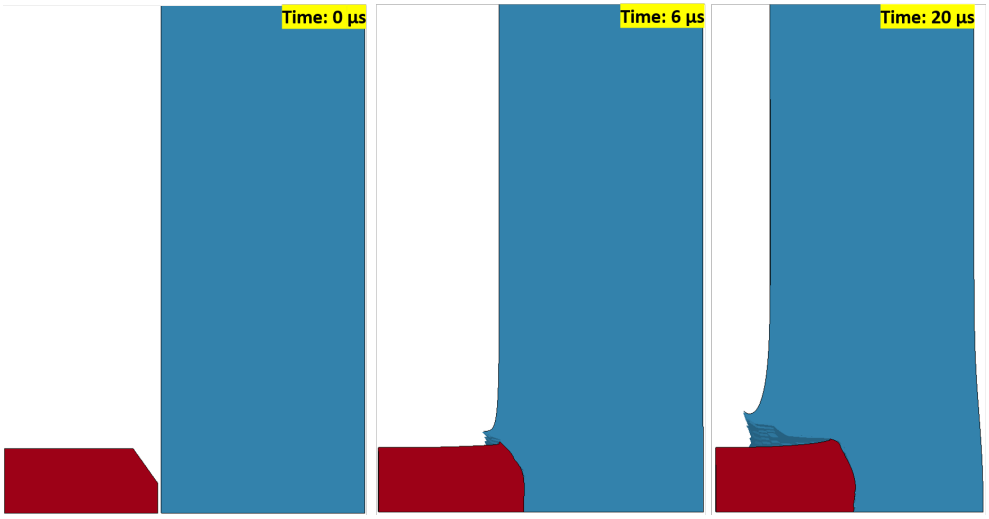

Figure A.1: A detailed display of the 31mm thickness 800m/s impact velocity perforation - (0μs - 20μs)

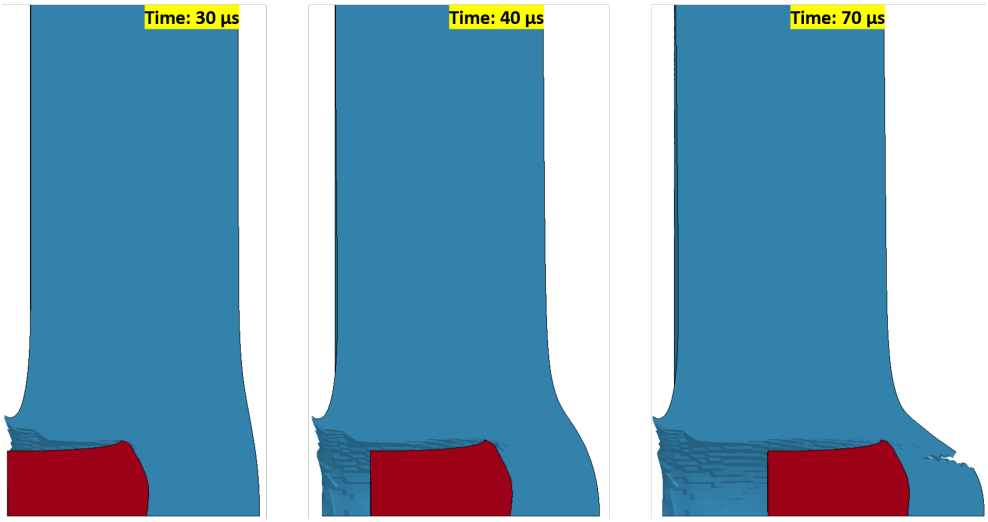

Figure A.2: A detailed display of the 31mm thickness 800m/s impact velocity perforation - (30μs - 70μs)

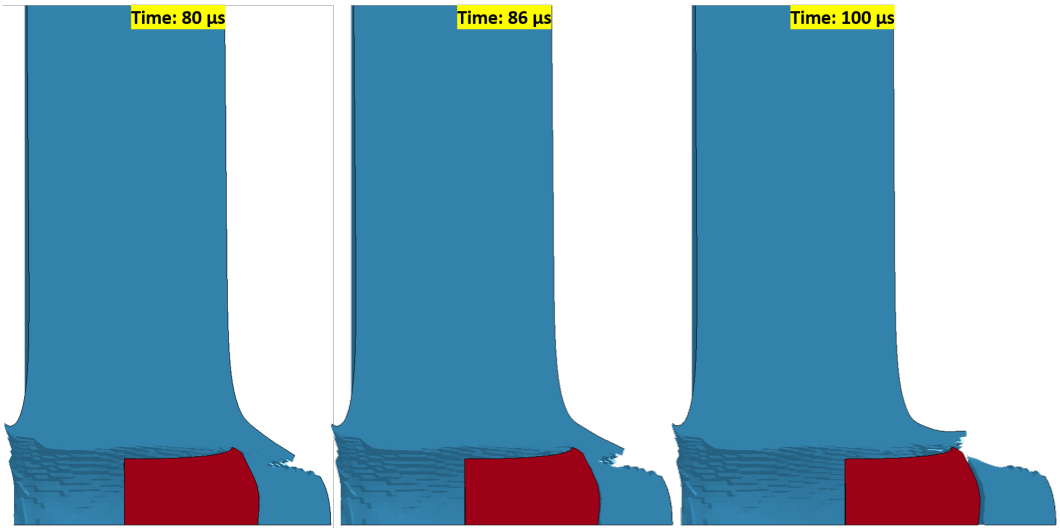

Figure A.3: A detailed display of the 31mm thickness 800m/s impact velocity perforation - (80μs - 100μs)

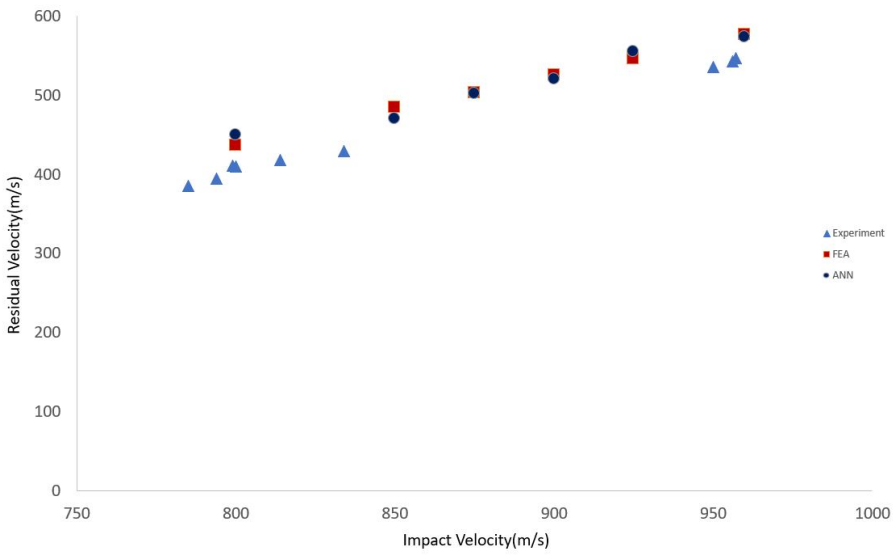

Figure A.4: Experiment, FEA and ANN results for 25.4mm thickness

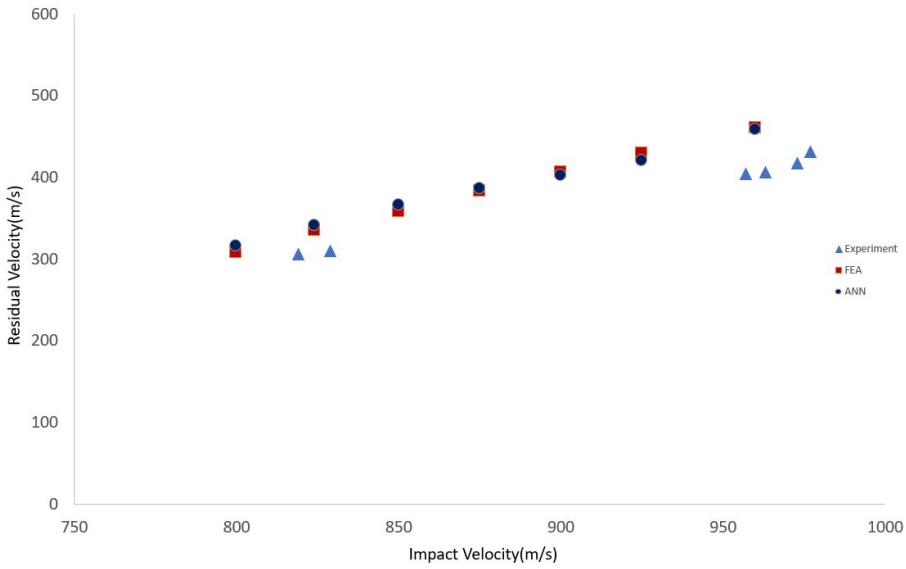

Figure A.5: Experiment, FEA and ANN results for 31mm thickness

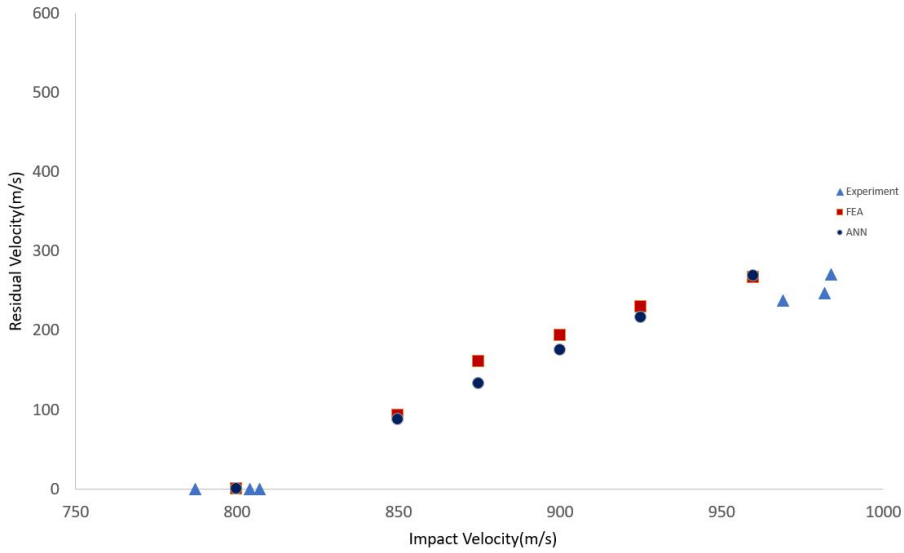

Figure A.6: Experiment, FEA and ANN results for 38mm thickness